Technical University of Munich
Department of Physics
Chair of Experimental Physics with
Cosmic Particles

Bachelor's Thesis

Calibration and Data Analysis for the Precision Optical Calibration Module

Martin Mocker

01st of April, 2022

First Examiner: Prof. Dr. Elisa Resconi
Second Examiner: Prof. Dr. Peter Fierlinger
Supervisor: Dr. Felix Henningsen

Abstract

Neutrinos are elusive particles that rarely interact with matter. The Ice Cube Neutrino Observatory at the South Pole encompasses a large volume of ice to detect Cherenkov light resulting from neutrino interactions. This experiment pioneered the observation of extraterrestrial high-energy neutrinos and will undergo two major extensions in the coming years. The IceCube Upgrade will deploy various new calibration light sources, including more than twenty Precision Optical Calibration Modules (POCAMs). This instrument is developed in our group as an ’in-situ, self-calibrating, isotropic, nanosecond calibration light source’. For the pre-deployment calibration of these POCAMs, two calibration setups have been developed. The POCAM calibration station measures the relative intensity, spectrum and time profile of several diodes and drivers in dependence of temperature and bias voltage. The main focus of this work was to transform and reduce this data to a format suitable for the IceCube Upgrade database. While the relative intensity can, in most cases, be fitted with a linear function, the spectrum and time profiles are described using a Gaussian fit and numeric approximations, respectively. For the latter, we describe two methods to approximate the profiles and compare their goodness-of-fit to find the best-describing technique. All of these data analyses, transformations and reductions are outlined in detail.

Contents

1 Neutrinos **1**

1.1 Fundamental properties . . . 1

1.2 Neutrinos in multi-messenger astronomy . . . 2

1.3 Astrophysical sources . . . 3

1.3.1 Solar neutrinos . . . 4

1.3.2 Atmospheric neutrinos . . . 5

1.3.3 Extraterrestrial high-energy neutrinos . . . 5

1.4 Interactions . . . 6

2 IceCube Neutrino Observatory **8**

2.1 Design . . . 8

2.2 Detection principle . . . 9

2.2.1 Cherenkov effect . . . 9

2.2.2 Event signatures . . . 10

2.3 Optical effects . . . 12

2.4 Future extensions . . . 14

2.4.1 IceCube Upgrade . . . 14

2.4.2 IceCube-Gen2 . . . 16

3 Precision Optical Calibration Module **17**

3.1 Design . . . 17

3.2 Flasher configuration . . . 18

3.3 Electronics and self-monitoring sensors . . . 20

3.4 Calibration . . . 21

3.4.1 Instruments and general procedures . . . 21

3.4.2 Calibration station . . . 23

4 Calibration station data analysis **26**
4.1 Intensity 27
4.1.1 Photodiode 27
4.1.2 Photomultiplier Tube 29
4.2 Wavelength 29
4.3 Time profile 33
4.3.1 Method 1: Volume levels 34
4.3.2 Method 2: Height levels 35
4.3.3 Comparison of both methods 36

5 Summary **46**

A Figures **48**

B Bibliography **54**

Chapter 1

Neutrinos

1.1 Fundamental properties

The Standard Model (SM) of particle physics includes six quarks with six flavours and six leptons with three flavours. Each lepton flavour consist of a charged partner (e^-, μ^- and τ^-) and an uncharged neutrino (ν_e, ν_μ and ν_τ). The neutrinos cannot interact via the electromagnetic or strong interaction, but only via the weak force, disregarding gravitation. Hence, they are difficult to be detected. In contradiction to the prediction by the SM, it is also known that neutrinos need to have a mass, due to neutrino oscillations, manifesting themselves in flavour changes [1]. In the theoretical realisation, a mixing-matrix U, called PMNS-matrix, is introduced as shown in equation 1.1. The flavour-eigenstates are relevant in weak processes, but they are a superposition of three mass-eigenstates $|\nu_1\rangle, |\nu_2\rangle$ and $|\nu_3\rangle$. Their different time evolutions during propagation lead to oscillations and a certain probability to detect a different flavour-eigenstate compared to the neutrino's creation [1]. The mass differences between the mass-eigenstates can be assessed, but their ordering is not fully resolved [2].

$$\begin{pmatrix} |\nu_e\rangle \\ |\nu_\mu\rangle \\ |\nu_\tau\rangle \end{pmatrix} = \begin{pmatrix} U_{e1} & U_{e2} & U_{e3} \\ U_{\mu 1} & U_{\mu 2} & U_{\mu 3} \\ U_{\tau 1} & U_{\tau 2} & U_{\tau 3} \end{pmatrix} \begin{pmatrix} |\nu_1\rangle \\ |\nu_2\rangle \\ |\nu_3\rangle \end{pmatrix} \tag{1.1}$$

1.2 Neutrinos in multi-messenger astronomy

Until the 1980's, the universe could only be probed with electromagnetic signals [3]. The field of multi-messenger astronomy (MMA) aims to combine observations of multiple signals from the same astrophysical processes. One early example is a neutrino signal coming from a gravitational collapse of a star in the Large Magellanic Cloud in 1987 [4]. Today, the used probes in MMA are photons, neutrinos, cosmic rays and gravitational waves [3]. For example, in 2017 gravitational waves and γ-rays coming from the same neutron star merger were detected independently by the LIGO-Virgo detector network [5] and the Fermi satellite [6], respectively.

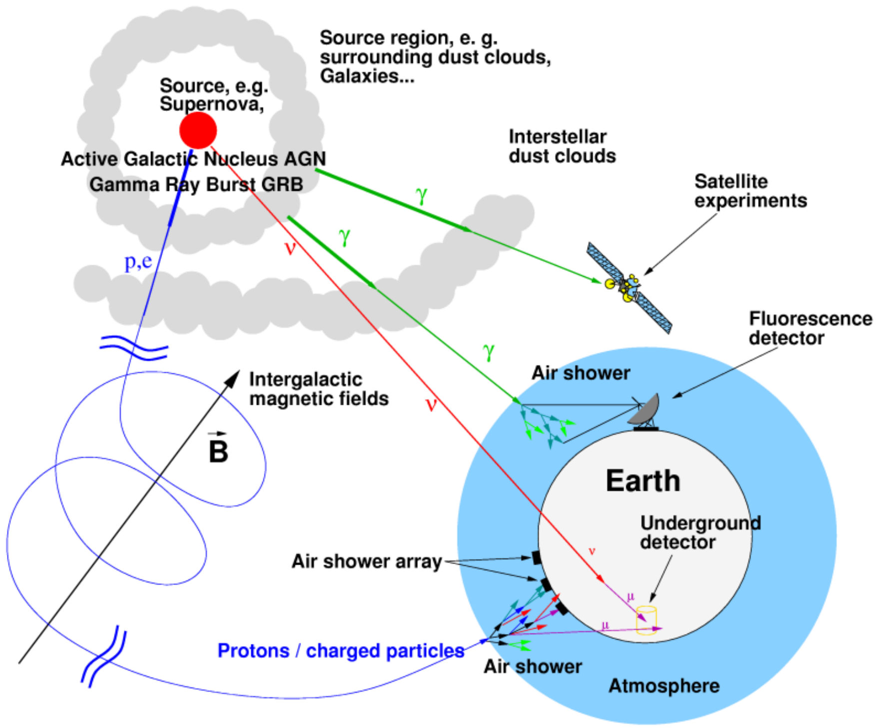

Figure 1.1: Overview of cosmic messengers showing the path and detection of cosmic rays, neutrinos and γ-rays. Only neutrino beams are not altered on their way to Earth. Figure taken from [7].

Figure 1.1 shows the path of different messengers on their way to Earth. As cosmic rays consist of charged particles, mainly protons [8], they get deflected by intergalactic magnetic fields. Therefore, it is usually not possible to determine their exact source. Uncharged particles, like neutrinos and photons, can be produced near the source (cf. chapter 1.3.3). They are not deflected on their way to Earth and would therefore allow an easier directional reconstruction. For γ-rays this proves difficult, as high-energy photons can be generated in various processes and their flux is reduced by e.g. interstellar dust [7]. Neutrinos could solve that problem, as they rarely interact with matter. The detection of high energy neutrinos and pairing with a source would help to better understand cosmic ray interactions [7].

However, it is not easy to identify the exact source of high-energy extraterrestrial neutrinos. Until today, there only have been two observations that point towards a neutrino emission associated with astrophysical sources. In 2017, a neutrino signal coming from the direction of the blazar TXS 0506+056 was detected by the IceCube Neutrino Observatory (c.f. chapter 2) matching in time a gamma ray flare from said blazar [9]. A follow-up analysis by the IceCube collaboration later identified blazars as the first possible source for high-energy extragalactic neutrinos [9]. Additionally, the active galaxy NGC 1068 has recently been unmasked as a possible neutrino source using several years of IceCube data [10].

1.3 Astrophysical sources

In general, there are various neutrino sources in the universe. Figure 1.2 shows a unified neutrino spectrum on Earth over a wide range of energies. All contributions are described briefly with emphasis on solar neutrinos from nuclear fusion, atmospheric neutrinos and extraterrestrial high-energy neutrinos.

The Cosmic Neutrino Background (CNB) is dominant in the lowest energy range. It consists of relic neutrinos that decoupled after the Big Bang, similar to photons in the Cosmic Microwave Background (CMB). Additionally, a neutrino flux that results from unstable isotopes and free neutrons that were left over after the Big Bang Nucleosynthesis (BBN) is shown. From 1 eV to 1 keV thermal solar neutrinos are dominant. They are created e.g. by plasmon decay, the compton process and electron bremsstrahlung [11]. The only terrestrial sources in the presented spectrum are reactors and radioactive isotopes present on Earth (geoneutrinos). Their flux strongly depends on location. The diffuse supernova neutrino background (DSNB) is made up of all collapsing stars in the visible universe [11].

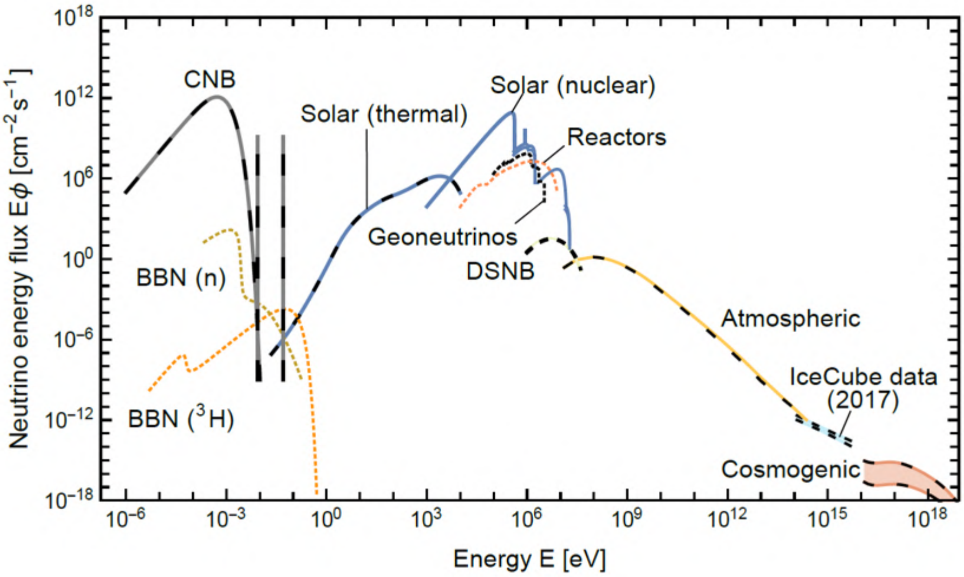

Figure 1.2: Neutrino flux (all flavours) on Earth as a function of energy including several sources. The spectrum is integrated over every direction. Solid and dotted lines are for neutrinos and antineutrinos, respectively. Lines with two colours are for both. Image taken from [11].

1.3.1 Solar neutrinos

The sun constantly undergoes nuclear fusion and emits electron neutrinos coming from different fusion cycles. The highest flux is expected from pp-chains which always start with the following process to create deuterium [11]:

$$p + p \rightarrow d + e^{+} + \nu_e \tag{1.2}$$

The average neutrino energy of this fusion is 0.267 MeV, while the highest neutrino energy coming from any cycle equals 18.778 MeV [11].

The sun is among the best measured and understood neutrino sources. Discrepancies in the solar electron neutrino flux lead to the theory of neutrino oscillations and they were eventually confirmed by the SNO experiment, which managed to measure the flux of all three flavours simultaneously [11].

1.3.2 Atmospheric neutrinos

When cosmic rays hit the atmosphere, secondary particles, mainly pions and kaons, are produced [11]. Their decays create (anti-)neutrinos via the following processes:

$$\pi^{\pm} \longrightarrow \mu^{\pm} + \nu_{\mu}\ (\bar{\nu}_{\mu})\ ,\ K^{\pm} \longrightarrow \mu^{\pm} + \nu_{\mu}\ (\bar{\nu}_{\mu}) \tag{1.3}$$

The (anti-)muons decay further.

$$\mu^{\pm} \longrightarrow e^{\pm} + \nu_{e}\ (\bar{\nu}_{e}) + \bar{\nu}_{\mu}\ (\nu_{\mu}) \tag{1.4}$$

Other occurring processes include:

$$K^{\pm} \longrightarrow \pi^{0} + e^{\pm} + \nu_{e}\ (\bar{\nu}_{e})\ ,\ K^{\pm} \longrightarrow \pi^{\pm} + \pi^{0}\ ,\ \pi^{0} \longrightarrow \gamma + \gamma \tag{1.5}$$

Up to 1 GeV the ratio $(\nu_e + \bar{\nu}_e) : (\nu_\mu + \bar{\nu}_\mu)$ equals 1:2, but at higher energies equation 1.4 becomes negligible and the ratio drops [11]. The spectrum as shown in Figure 1.2 can be described with an inverse power-law and atmospheric neutrinos provide a background for detectors of high-energy astrophysical neutrinos like IceCube [11].

1.3.3 Extraterrestrial high-energy neutrinos

High-energetic protons from cosmic rays mainly undergo the following interactions in astrophysical shock fronts [12]:

$$p + \gamma \longrightarrow \Delta^{+} \longrightarrow p\ (n) + \pi^{0}\ (\pi^{+}) \tag{1.6}$$
$$p + p \longrightarrow p + p\ (n) + \pi^{0}\ (\pi^{+}) \tag{1.7}$$

Afterwards, the decays listed in equations 1.3 - 1.5 lead to a flux of photons and neutrinos. The latter are in the TeV to PeV range and are detectable by e.g. IceCube. Due to large travel times and neutrino oscillations it is expected that all three flavours arrive on earth in equal amounts [12]. There are many sources able to generate high-energy cosmic rays and in consequence neutrinos. A short description of several galactic and extragalactic sources can be found in [7]. This work will give a short overview of the most efficient neutrino emitters following [11].

Gamma ray bursts (GRBs) are among the most energetic events in the universe. The main production channels for neutrinos are pγ-interactions of high-energetic cosmic rays [11]. So far, no known GRBs overlapped with neutrino events in IceCube, but low-luminosity GRBs could partially explain a diffuse high-energy neutrino flux in the detector [11].

An Active Galactic Nucleus (AGN) is the bright centre of a galaxy. It is a very powerful emitter of photons and neutrinos, which are generated after pγ-interactions of cosmic rays [11]. Blazars are AGNs with a jet pointing towards earth and are promising cosmic accelerators that could explain a large majority of the flux in IceCube. This is shown in [13] where some blazar-studies are presented. Furthermore, the first localised emission of astrophysical neutrinos likely originated from a blazar.

Star-forming galaxies (SFGs) have an enhanced star formation activity. They are a likely neutrino source due to pp-interactions of cosmic rays. Approximately 55% of all galaxies can be assigned to this type [11]. Their high abundance in the universe contributes to the modelling-result that a detection of a neutrino emission from a specific SFG with IceCube is and will be highly unlikely [14].

At the right end of the spectrum, cosmogenic neutrinos are postulated. They are likely produced when ultra-high-energy cosmic rays, with energies up to 10^{20} eV, interact with the CMB and the extragalactic background light [11]. Neutrinos can then be produced via equation 1.6.

1.4 Interactions

Neutrinos can take part in weak processes with e.g. a nucleon N. Important matter-interactions of neutrinos in detectors are charged current (CC) and neutral current (NC) processes [15]. They are mediated via a $W^{\pm}$ and Z^0 boson, respectively. In a CC interaction the incoming neutrino with flavour ℓ changes to the corresponding lepton. On the contrary, an incoming neutrino is unchanged after a NC interaction. In the exemplary processes below, X denotes hadronic secondaries, e.g. a hadronic cascade.

$$\nu_\ell + N \longrightarrow \ell + X \quad (CC) \tag{1.8}$$

$$\nu_\ell + N \longrightarrow \nu_\ell + X \quad (NC) \tag{1.9}$$

Figure 1.3 shows the cross sections of (anti-)neutrinos in CC and NC processes. In both cases the cross section is very small, but rises with energy. In the depicted energy range it can also be seen that a CC interaction is favoured compared to a NC interaction.

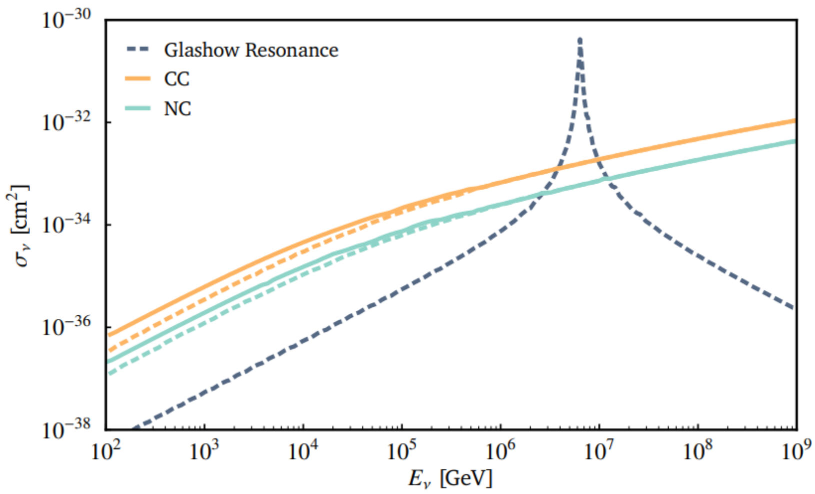

Figure 1.3: Neutrino cross sections as a function of energy for CC and NC processes. Full lines represent neutrinos and dashed lines antineutrinos. A special case, the Glashow resonance, is also shown. Figure taken from [15].

The highest cross section is achieved in the Glashow resonance at around 6.3 PeV. In this interaction a W$^-$ boson can be produced via the following process [15]:

$$\bar{\nu}_e + e^- \longrightarrow W^- \longrightarrow X \tag{1.10}$$

Chapter 2

IceCube Neutrino Observatory

2.1 Design

The IceCube Neutrino Observatory is located at the geographical South Pole and consists of 5160 digital optical modules (DOMs) on 86 strings. In total, these strings encompass 1 km^3 of ice in a depth of 1450 m to 2450 m [15]. Figure 2.1 gives a detailed overview of the structures in and on top of the ice. IceCube aims to observe neutrinos by detecting Cherenkov light (c.f. chapter 2.2.1) of neutrino interaction products [16]. Due to the low cross sections, as seen in figure 1.3, only the large volume of the experiment allows to observe these elusive particles with statistical significance [16].

The primary In-Ice Array consists of 78 strings evenly spaced 125 m apart in an hexagonal shape on a triangular grid. This configuration and the 17 m vertical distance between the DOMs have been chosen to meet the scientific requirements of detecting astrophysical neutrinos in and above the TeV range [16]. Eight additional strings form the denser DeepCore region where the energy threshold for the detection of neutrinos is decreased to 10 GeV, compared to approximately 100 GeV for the rest of the detector [16]. The 81 IceTop stations are used to measure air showers and can act as a veto for e.g. down-going muons [16].

Each DOM is encapsulated in a glass pressure sphere and contains a downwards-facing Photomultiplier Tube (PMT) of 25 cm diameter able to detect Cherenkov light [16]. The top half includes electronics and twelve 405 nm light emitting diodes (LEDs) with adjustable pulse width and intensity [16]. For calibration purposes these LEDs can artificially illuminate the detector volume. Similar calibration techniques are commonly used in other large-scale neutrino detectors [15].

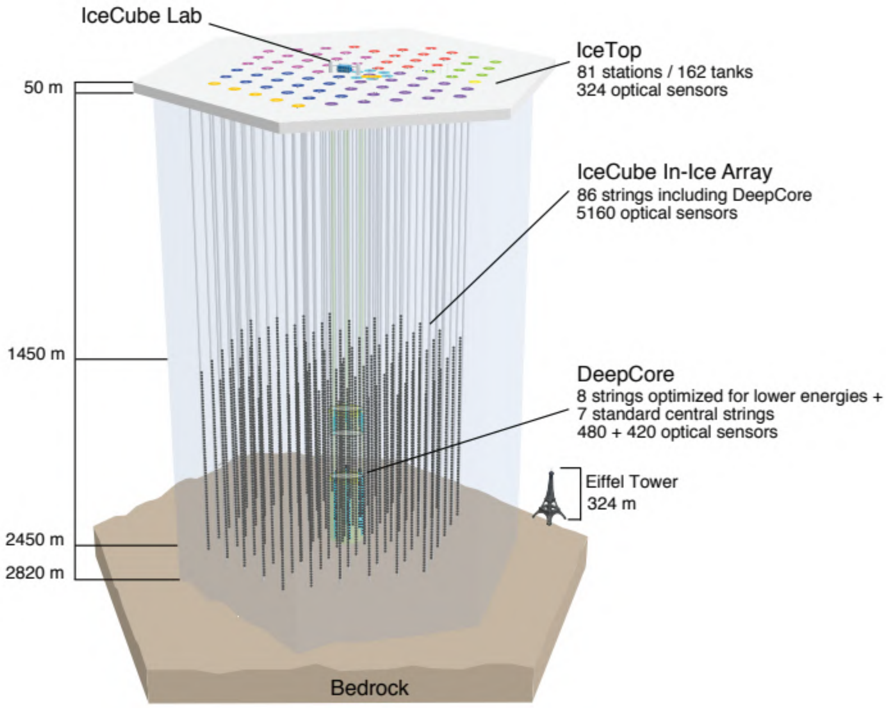

Figure 2.1: Arrangement of the strings and optical modules in the IceCube detector. The whole In-Ice-Array, DeepCore and IceTop are shown. Figure taken from [16].

2.2 Detection principle

2.2.1 Cherenkov effect

Charged particles, travelling through matter with a speed greater than the speed of light in the medium, emit Cherenkov radiation in a cone-like shape [17] as illustrated in figure 2.2. The opening angle θ can be calculated according to equation 2.1 where v is the speed of the charged particle, c is the speed of light in vacuum and n is the refractive index of the respective medium [17].

$$\cos\theta = \frac{1}{\beta n}, \ \beta = \frac{v}{c} \tag{2.1}$$

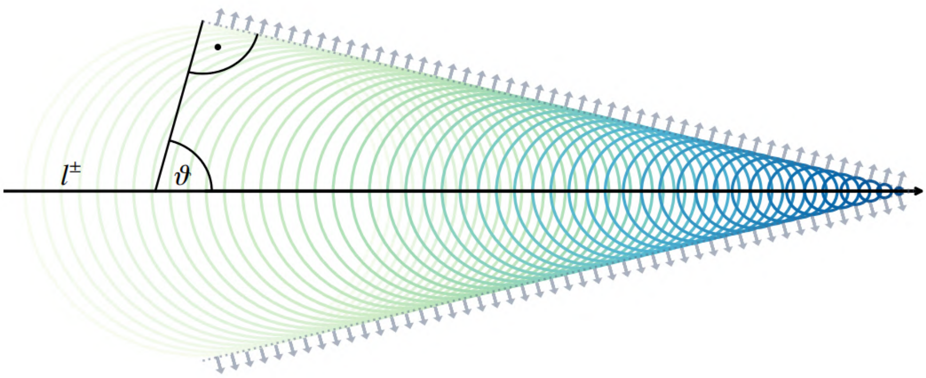

Figure 2.2: A charged lepton travels from left to right and emits Cherenkov light under the angle θ. Figure taken from [15].

In neutrino detectors, the Cherenkov effect is important when a high-energy neutrino transfers a significant amount of energy to a lepton in a CC interaction [8]. The known geometry of Cherenkov radiation and a sufficient number of photon detections with a good spatial and time resolution allow, in general, a directional reconstruction of the primary neutrino [18]. However, the deep-inelastic scattering of neutrinos induces particle showers, which are an additional source for photons from the Cherenkov effect and other electromagnetic processes [19]. There are various methods where this light yield of different particles and showers can be used to reconstruct to energy of the initial neutrino [19].

2.2.2 Event signatures

In IceCube, high-energy events initiated by neutrino CC interactions can be usually described as either cascades or tracks [19]. The former result from an electron neutrino interacting inside the detector volume. The latter show the distinct path of a secondary muon produced after an interaction of a muon neutrino. In principle, there is also a third type, called a double bang, induced by a primary tau neutrino [19]. All three types are explained further in this chapter and the expected signatures are simulated in figure 2.3. A NC interaction also produces a cascade, but the neutrino keeps most of its energy. This is not the case for a CC interaction where the majority of the incoming neutrino energy is deposited in light-producing particles [19].

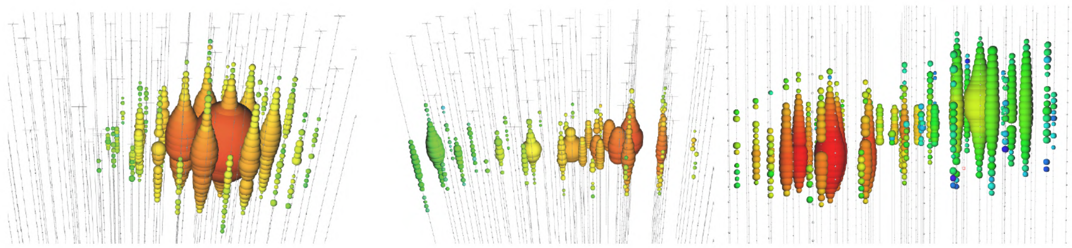

(a) *Cascade* **(b)** *Track* **(c)** *Double bang*

Figure 2.3: Characteristic neutrino events in IceCube. Each coloured sphere is a DOM that was hit by photons. A bigger sphere means a higher count and the colour represents time. Red equals early. Figure adapted from [20].

From equation 1.8, we already know that a hadronic shower is induced in the detector after a CC interaction. If an electron is produced it quickly loses energy inside the detector material and ignites a second, overlaid shower near the first neutrino vertex [19]. These particle showers have a typical length of 10 m and are, hence, not resolvable and indistinguishable from cascades after NC interactions [19]. The propagation length does not change significantly with the energy as seen in figure 2.4. The directional reconstruction of a cascade has a resolution of $10°$ to $15°$ [18].

Muons create tracks inside the detector, as they have a relatively long propagation length in ice (c.f. figure 2.4). It is in the range of the detector size or above, considering the relevant energy thresholds of the In-Ice Array and DeepCore. The tracks coming from high-energetic muons can be characterised in different types. If a neutrino vertex lies inside the detector volume we have a starting-track event and otherwise it is called through-going [13]. Down-going tracks are another important event type. They are mostly induced by atmospheric muons and are about 10^6 times more likely to be detected than a track induced by a muon-neutrino [20]. Above some TeV, the resolution from the directional reconstruction of a track is a few tenths of a degree [18]. This makes them suitable candidates to find astrophysical sources. Moreover, it should be noted that the energy reconstruction of a track is worse compared to a cascade, as the energy losses of a muon occur randomly, which makes them difficult to quantify [15].

A signal induced by a tau neutrino can be described as a double bang. One cascade is produced at the neutrino interaction vertex and the other one when the lepton decays inside the detector volume, due to its relatively short life-time [13]. From figure 2.4, it can be concluded that a double bang can only be resolved at energies in the PeV-range. At low energies they are nearly indistinguishable from cascades [13]. Recently, two double bang candidates were identified, being consistent with the expected flavour ratios (c.f. chapter 1.3.3) of astrophysical neutrinos [21].

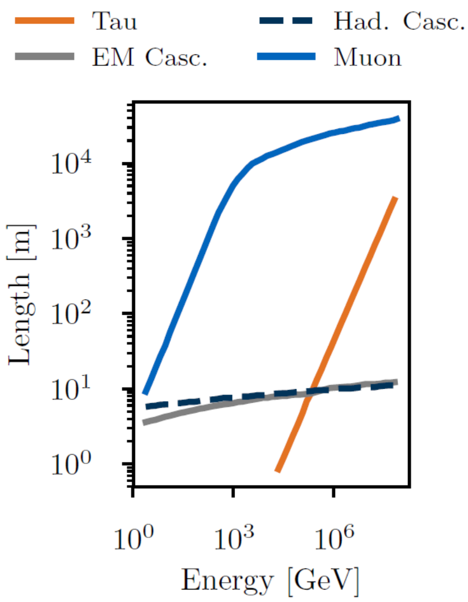

Figure 2.4: Energy-dependent propagation length of different particles and cascades. The graphs are for water, but they apply almost similar for ice. Figure taken from [13].

2.3 Optical effects

From chapter 2.2 it is clear that the optical properties of the South Pole ice play an important role in the detection of neutrinos. The detector medium offers good optical qualities, specifically a ,large absorption length [16]. It can be described with the quantity ℓ_a and can be used as a parameter in the exponential Lambert-Beer law (c.f. equation 2.2) together with the scattering length ℓ_b [15]. These two lengths are needed for the most basic description of the photon propagation inside neutrino detectors in water and ice [22]. Considering N_0 original photons, the law calculates the number of photons that are not absorbed or scattered after a path of length d.

$$N(d) = N_0 \cdot \exp\left\{-\frac{d}{\ell_{a,b}}\right\} \tag{2.2}$$

Table 2.1 shows the longer absorption length in ice compared to water, but it can also be seen that the scattering length in ice is shorter. Generally, the absorption length in IceCube allows a relatively wide spacing of strings, while scattering may obscure timing information and complicates e.g. the distinction of different cascades [15].

Table 2.1: Absorption lengths ℓ_a and scattering lengths ℓ_b for different detector media. The values for water depend on season and site. Table adapted from [22].

Site	ℓ_a [m]	ℓ_b [m]
Lake Baikal (1 km depth)	18 - 22	150 - 250
Ocean (1.5 km depth)	40 - 70	200 - 300
Polar ice (1.5 km - 2 km depth)	$\sim$ 95	$\sim$ 20
Polar ice (2.2 km - 2.5 km depth)	100	30 - 40

Apart from scattering effects, the major systematics in IceCube arise from the optical properties of different ice types in the detector [18]. They are briefly explained below.

All ice between the strings is called bulk ice. Here, the variations of optical parameters are mainly driven by different dust concentrations [23]. A corresponding plot of ℓ_a^{-1} and ℓ_b^{-1} is shown in figure 2.5 where it can be seen that the most unfavourable values are in a dust layer between 1950 m and 2100 m. Between 2000 m and 2100 m this region contains no DeepCore modules [16].

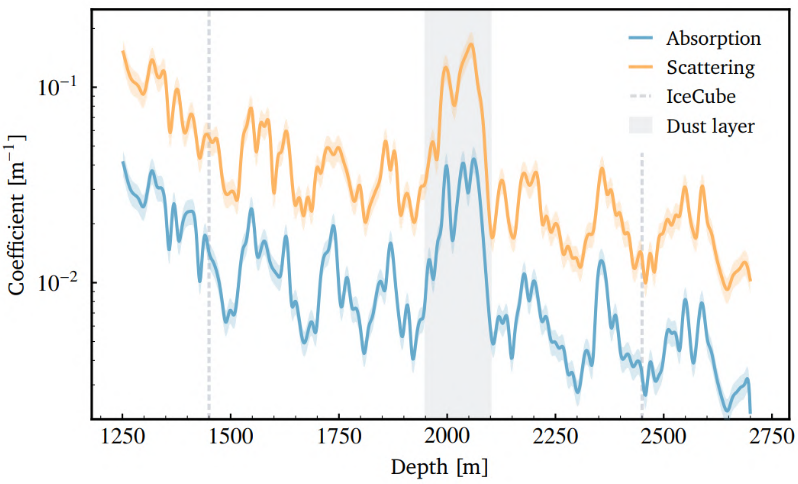

Figure 2.5: Bulk ice properties as a function of depth. The plot also includes the estimated 10% uncertainty for the absorption and scattering parameters. Figure taken from [15] and data courtesy of the IceCube Collaboration.

When a drill hole refreezes after the deployment of a string, the cylindrical hole ice forms. It has different optical properties than the bulk ice and is less understood [24]. One in-situ observation of the hole ice was conducted with a camera deployed in a drill hole [24]. It could differentiate between a clear outer region and a ∼8 cm wide inner region with a significantly decreased scattering length [24]. Figure 2.6 shows the phenomenon. The study and modelling of the hole ice is an active topic within the IceCube collaboration [15].

Figure 2.6: Open drill hole (left) and the camera view after refreezing (right). A grey ice column is clearly visible on the right. Figure adapted from [25].

2.4 Future extensions

There are two planned extensions for the IceCube neutrino observatory with specific scientific goals as listed in [26]. These mainly include further calibration, decreasing the energy threshold to measure fundamental neutrino parameters and advancing the detection of astrophysical neutrinos in a higher energy range than before.

2.4.1 IceCube Upgrade

The IceCube Upgrade will include low energy installations and new calibration modules [15]. It will provide seven new strings with approximately 700 sensors of different kinds that are planned to be deployed in the antarctic summer of 2022/23 [27]. An overview regarding the location of the new strings and the vertical spacing of the new modules can be seen in figure 2.7.

Several new systems and devices will be installed, but the majority consists of 'multi-PMT Digital Optical Modules' (mDOMs) and 'Dual optical sensors in an Ellipsoid Glass for Gen2' (D-Eggs) [15]. This thesis will concentrate on on the 'Precision Optical Calibration Module' or POCAM (c.f. chapter 3). It is a calibration instrument with an isotropic emission profile that will enable more precise measurements compared to the currently used LEDs [28]. By means of an in-situ self-calibration the POCAM aims to reduce the uncertainties on optical parameters (c.f. figure 2.5) to a few percent [29]. The module is currently being developed in our group [30] and it is planned that more than 20 individual modules will be deployed in the IceCube Upgrade [29].

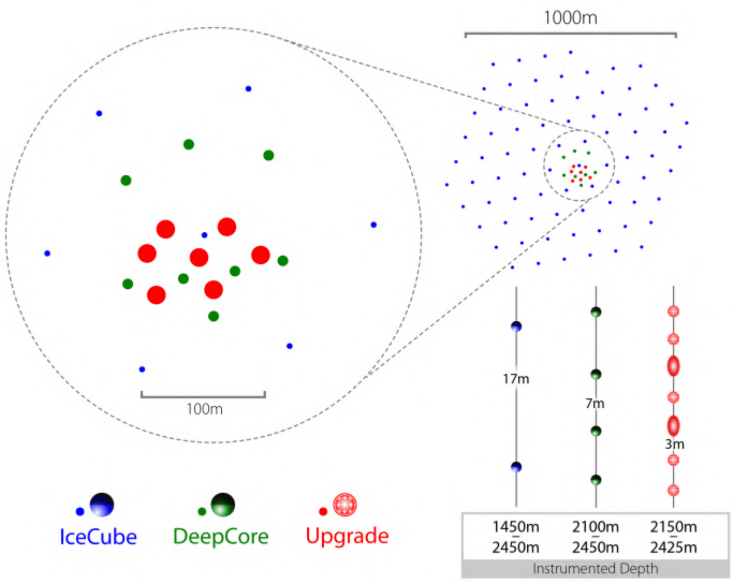

Figure 2.7: Layout of the new strings inside the DeepCore region of the In-Ice Array. The Upgrade will provide the densest clustering of modules inside the detector. Figure adapted from [27].

With the deployment of new, highly efficient and densely packed sensors it will be possible to reduce the energy threshold for the detection of neutrinos to about 1 GeV [27]. Additionally, the deep location provides low rates of detector noise, allowing competitive measurements of neutrino oscillation parameters, e.g. θ_{23} and Δm^2_{31} [27]. Here, θ_{23} is one of three mixing angles included in the mixing matrix from equation 1.1 and $\Delta m^2_{31} = m^2_3 - m^2_1$ is the squared mass difference of the corresponding mass-eigenstates [1].

2.4.2 IceCube-Gen2

IceCube-Gen2 increases the In-Ice Array to a total volume of $8\,\mathrm{km}^3$ and combines it with a $500\,\mathrm{km}^2$ radio array on the surface to detect ultra-high-energy neutrinos [31]. A schematic overview of both structures can be seen in figure 2.8. The extension will be sensitive up to energies of 10^9 GeV. It aims to detect isolated, bright neutrino sources and less luminous populations of sources with a relevant significance that is not reachable with the current detector specifications [31].

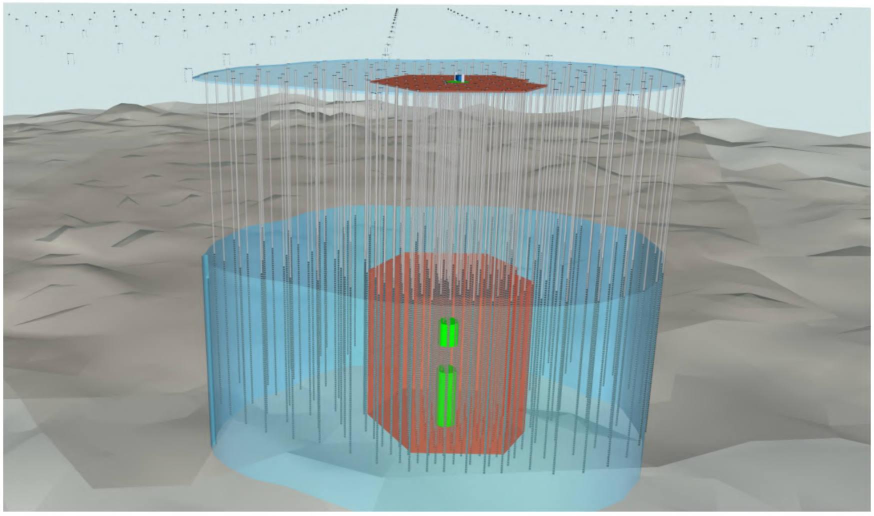

Figure 2.8: Existing In-Ice Array (red) with the DeepCore region (green). The blue volume and the surface arrays are extensions in IceCube-Gen2. Figure taken from [31].

Chapter 3

Precision Optical Calibration Module

We introduce the Precision Optical Calibration Module (POCAM) as an 'in-situ, self-calibrating, isotropic, nanosecond calibration light source that emits flashes of adjustable intensity and pulse duration' [29]. We explain these relevant characteristics in this chapter. The presented module is the third iteration [15]. The first version was tested in the Gigaton-Volume-Detector in Lake Baikal [32] and the second one in the Pacific Ocean where a new neutrino telescope is planned [33].

3.1 Design

An illustration of a full module and an overview of one hemisphere are shown in figure 3.1 and 3.2, respectively. The instrument measures about 40 cm in length and 13 cm in diameter [34]. The cylindrical titanium pressure housing was manufactured by Nautilus Marine Service GmbH and is expected to withstand temperatures down to $-55\,^{\circ}\mathrm{C}$ and pressures up to roughly 1000 atm [34]. Several evaluations, including vibration and shock tests, confirmed that the module is suitable for the harsh conditions in deep neutrino detectors in water or ice [34].

A semi-transparent sphere made of *polytetrafluorethylen* (PTFE or teflon) is used to create isotropic light pulses and it was determined that a specially produced optical PTFE produces the best results [29]. In figure 3.2 it can be seen that the whole diffuser is made up of the sphere and a plug. The latter acts as a pre-diffuser and is important to prevent intensity variations due to influences of the emitting surface [29]. Additionally, measurements and simulations suggest that a placement of the integrating sphere above the centre of the glass hemisphere, with an offset in the range of a few millimetres, could further improve the isotropy [34]. Figure A.1 shows an angular emission profile for one hemisphere and the virtual sum where the same data is used to mimic the second hemisphere. It can be seen that there are only small deviations from full isotropy. In simulations it was concluded that the former method, where only one hemisphere is truly measured, is valid and that the assumption of a point-like source is true given the future string-spacing in IceCube Upgrade [35].

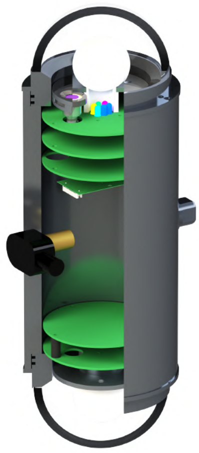

Figure 3.1: Full view of a module. Figure taken from [15].

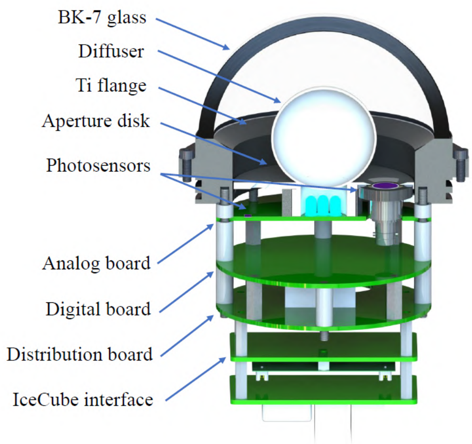

Figure 3.2: Flange cross-section and sub-components. Figure taken from [34].

3.2 Flasher configuration

The standard emitter type of the POCAM are LEDs which generally perform best in a range of 400 - 470 nm [29]. As a standard pulse driver, a Kapustinsky circuit [36] is used and the corresponding diagram is shown in figure A.2. It is able to produce light pulses in the nanosecond range and two configurations have been chosen to create a default and a fast version with 4 - 8 ns and 1 - 3 ns full width at half maximum (FWHM), respectively [34]. In the POCAM two equal Kapustinsky drivers that are switchable between fast/default are used for one 405 nm and two 465 nm LEDs [34]. The latter are of the same model and always flash together and are therefore treated as one LED.

Additionally, a laser diode (LD) driver, based on [37], is used to enable pulses with a relatively high intensity and with a FWHM that can be tuned in the range of approximately 1.5 - 35 ns [34]. A general diagram of such a circuit is shown in figure A.3. We will also refer to this driver as a LMG. It was chosen that the LD-type driver is used for a 405 nm, 450 nm and 520 nm LD and one 365 nm LED. The flashing of the latter is possible as the LD circuit provides large enough currents to generate significant intensity [34]. Measurements suggest that the LDs are able to generate 10^{10} - 10^{11} photons per pulse [34] and they are therefore suitable for an application in IceCube as they can illuminate sufficiently large detector volumes [29].

In general, the LD driver has the slight disadvantage of longer pulse widths, but it produces the largest intensities followed by the default and fast Kapustinsky driver [35]. Figure 3.3 shows this comparison. The intensity is measured in dependence of the adjustable bias voltage V_{CC}. Figure 3.4 illustrates the connections between the available drivers and diodes in the POCAM. Both circuits are included twice to increase redundancy [34]. In total, the used setup gives 2·2·2 different possibilities to flash a diode using a Kapustinsky driver and 2·4 for the LD driver. However, we assume that both drivers of the same type produce equivalent results and differentiate between eight cases.

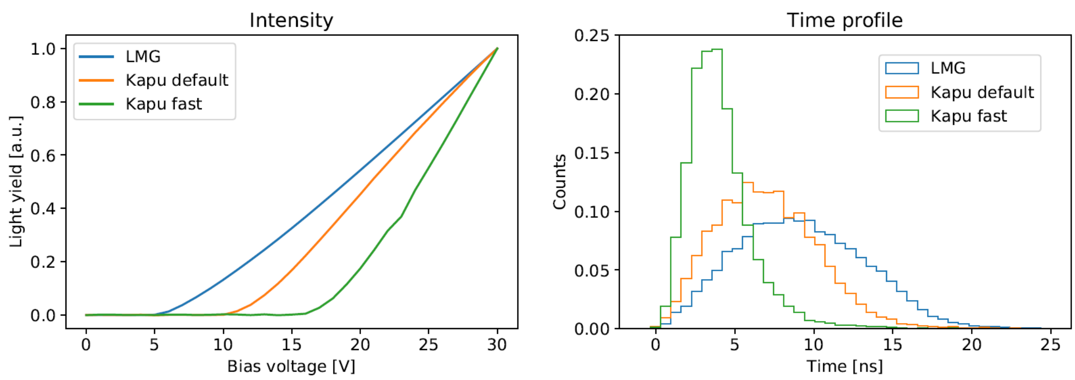

Figure 3.3: Left: Relative intensities for three flashers. LMG denotes the LD-type. It starts flashing at the lowest bias voltage followed by the default and fast Kapustinsky driver. Right: Time profiles for three drivers and a bias voltage of 30 V. The LMG was tuned to a FWHM of 15 ns. For all measurements the respective 405 nm diode was used. Figure taken from [35].

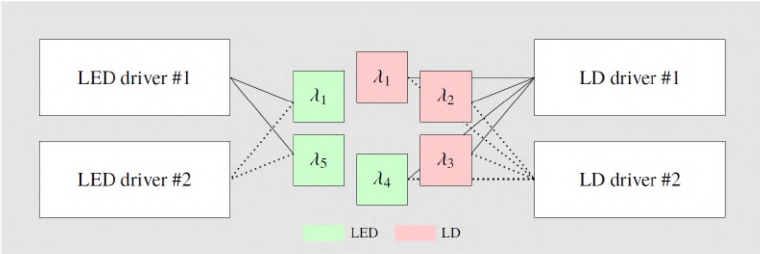

Figure 3.4: Schematic layout of the used drivers and diodes in the POCAM. For the respective wavelengths refer to the text. Figure taken from [34].

3.3 Electronics and self-monitoring sensors

All diodes and flasher circuits are located on an analog board (c.f. figure 3.2). There, the placements of the diodes was chosen in a way that all of them are as close to the centre of the board as possible, just below the PTFE sphere [35]. This is illustrated in figure 3.5 where the three LDs and LEDs can be seen in the middle. The two LEDs right of the centre are the ones driven by the Kapustinsky. Accordingly, in figure 3.6 where the bottom of the analog board is shown, the two respective circuits are located left of the centre.

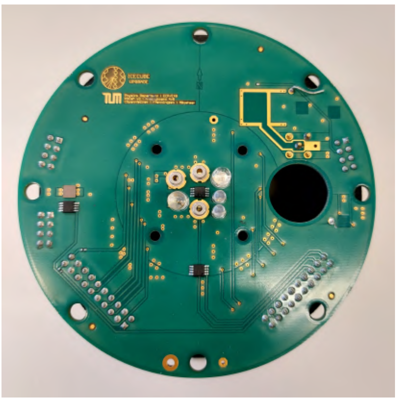

Figure 3.5: Top of the analog board.

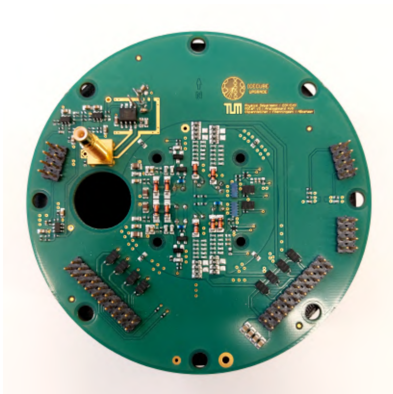

Figure 3.6: Bottom of the analog board.

From figure 3.2 it can also be inferred that the POCAM houses two photosensors per hemisphere with one of them being located directly on the analog board. Certain solid angles for both devices are provided by an aperture disk [34] and holes therein. The used sensors are a Silicon-Photomultiplier (SiPM) and a photodiode (PD) with which we provide two in-situ self-calibration devices that precisely measure the time onset and intensity of light pulses [29]. These measurements can also be used to monitor intensity fluctuations that may occur during a module's lifetime [34]. The necessity for two devices is explained with the different reachable intensities spanning almost five orders of magnitude where the SiPM and PD measure in the low- and medium- to high-intensity regime, respectively [15].

In each hemisphere below the analog board, a digital board is located. As its main function it controls the analog board, e.g. the bias voltage, all drivers and their selection, via an field-programmable gate array (FPGA) [15]. The configuration possibilities extend also to the self-calibration sensors and the board hosts an SD-card for temporary storage of the respective data [15]. The digital board has two holes similar to the one in the analog board. This is due to the length of the PD, which is larger than the distance between both boards, and the cable that connects the PD to the analog board [35].

A distribution board also hosts an FPGA and provides power to all necessary components in the previous boards [15]. As it is connected to both digital boards and only exists once per module, redundancy is of great importance and e.g. all voltage generation circuits are included twice [15]. At last, the IceCube Interface Board manages the connection of the module to the whole detector, including clock, power and data-streams [34]. Here, all different calibration devices use an identical board version that also includes g- and B-field sensors to determine the module's orientation [15].

3.4 Calibration

3.4.1 Instruments and general procedures

The first introduced calibration instrument is the POCAM Calibration Station. Throughout this work we will refer to it as POCAS or calibration station. With this setup, we calibrate the self-monitoring sensors and general light pulse properties, specifically relative intensity, wavelength spectrum and time profile, in dependence of temperature and other parameters [34], most importantly the applied bias voltage. As seen in figure 3.7, the setup mainly consists of a freezer housing the relevant POCAM components and a dark box encasing the dedicated sensors. Since the analysis presented in this thesis relies only on POCAS data, we give a detailed description of the station in chapter 3.4.2.

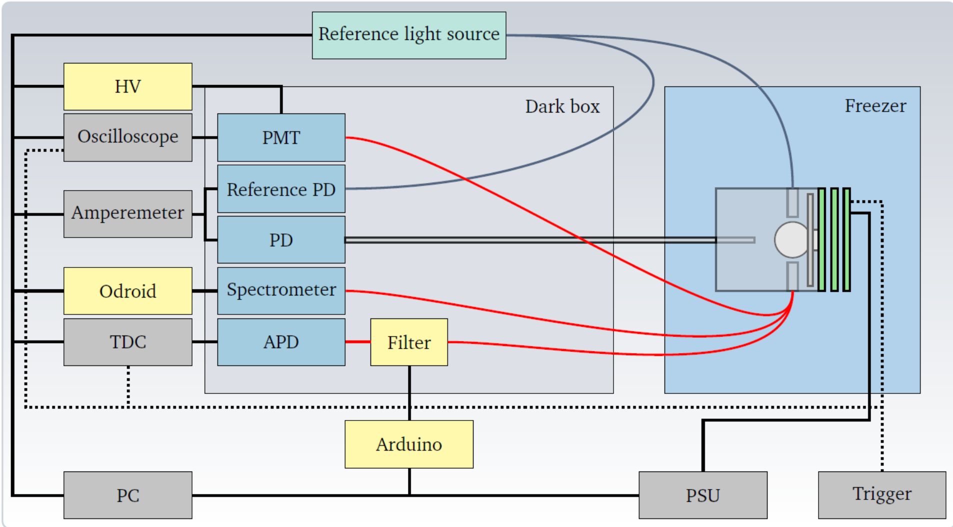

Figure 3.7: Schematic overview of the current calibration station setup to measure general light pulse properties. Relevant components are explained in chapter 3.4.2. Figure taken from [15].

The second setup is the Angular Calibration Station or ANGCAS shown in figure 3.8. It is used to measure the angular emission profile such as figure A.1. It consists of a 1.40 m long dark box with a PD on one end and a two-axis rotation stage on the other end [34]. On the latter, a POCAM hemisphere can be attached including all optical components and the analog board. However, an optimised illumination board is used. It hosts the same emitter configuration as figure 3.5, but allows a switchable continuous mode [15].

The Rotation Calibration Station is a third, planned setup. It consists of a steel frame where a POCAM can be mounted and rotated in water or air [15]. A model is shown in figure 3.9. Apart from the calibration of the field sensors on the IceCube Interface Board (c.f. chapter 3.3), the main task of the setup is to verify a dedicated simulation framework that predicts the module's emission profile in different optical media [15].

The general calibration procedure can be found in [15] and is briefly sketched here. At first, the flashers and their emission profiles will be characterised using the POCAS and ANGCAS, respectively. In both measurements only relative intensities are quantified and the absolute calibration is done by exchanging the PD in the ANGCAS with one that was precisely calibrated by the National Institute of Standards and Technology (NIST). Afterwards, a module's orientation will be calibrated with the Rotation Calibration

Station and some modules will be submerged in water to verify the emission profile in this medium. Taking into account various systematics effects, it is expected that the absolute intensity, spectrum and time profile can be calibrated with roughly 4%, 1 nm and 0.2 ns accuracy, respectively [15, 34].

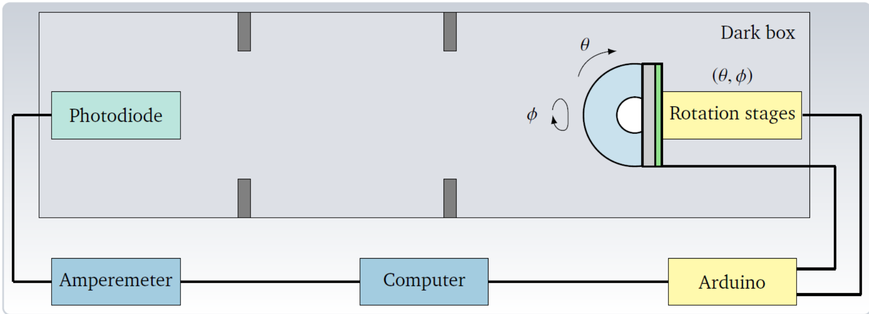

Figure 3.8: Schematic overview of the ANGCAS to measure the emission profile in dependence of two angles. Figure taken from [15].

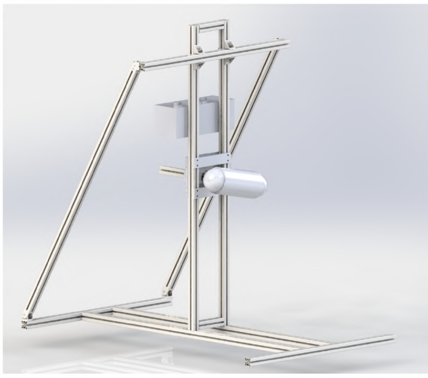

Figure 3.9: Virtual model of the rotation stage where a whole module can be rotated in water or air. Figure taken from [35] and image courtesy of L. Geilen.

3.4.2 Calibration station

Inside a freezer that can be cooled down to −75 °C, the diffuser, aperture disk and subsequent electronics are mounted [34]. As seen in figure 3.10, the mounting includes a metal cylinder that is put on the PTFE sphere. Through holes, optical fibres and a quartz rod can be attached in direct vicinity of the sphere. The setup in figure 3.7 shows all connections from and to the sphere.

Figure 3.10: Left: Mounting setup and inserted POCAM components inside the freezer. Right: Cross-section of the diffuser and the metal cylinder. The connections sit directly on the sphere's surface. Figures taken from [15].

To measure intensity, a quartz rod and an optical fibre lead to a PD and a PMT, respectively. Originally, the latter should cover the low intensity regime, but the rod allows the PD to detect also relatively dim light pulses [15]. Therefore, we use the PD for the whole intensity spectrum and only operate the PMT at low intensities for verification purposes [35].

Additionally, a different PD measures a reference light source and one fibre connects the latter directly to the PTFE sphere inside the freezer. With this setup we can quantify temperature-dependent differences in the coupling to the PTFE sphere [15]. To do this, we switch off all emitters, turn on the reference light source and compare the measured intensity of the reference PD (I_{ref}) with the detected light that passes through the PTFE sphere and then through the quartz rod ($I_{ref,rod}$). We can then calculate the following ratios and multiply the correction factor $\alpha_{corr}(T)$ to the measured intensity of a certain diode.

$$\alpha(T) = \frac{I_{ref,rod}(T)}{I_{ref}} \;, \; \alpha_{corr}(T) = \frac{\alpha(T_{room})}{\alpha(T)} = \frac{I_{ref,rod}(T_{room})}{I_{ref,rod}(T)} \tag{3.1}$$

The intensity from the reference source is assumed to be constant with variations smaller than 0.4 % [35]. We also note that both PDs are of the same type and dark measurements with all sources of light switched off are conducted beforehand [15].

One optical fibre leads from the freezer to a Hamamatsu C12880MA spectrometer [38] that provides 288 spectral bins in a range of 340 - 850 nm. Similar to the PD we perform a dark measurement to correct the actual measurement with the emitters [15]. To measure the time profile with reference to a trigger, we use an Avalanche Photodiode (APD) namely the IDQ ID100 [39] with a temporal resolution of 40 ps. As we want to count single-photons to not skew the profile, we put a neutral density filter wheel in front of the APD to ensure single photon hits with a probability close to one [15].

The data from all instruments is commonly depicted in the plots shown in figure 3.11. We use the 405 nm LED and the default Kapustinsky driver as an example. For the PD and the PMT, one plot depicts the relative intensities for different temperatures in dependence of the bias voltage. For the spectrum and the time profile, we need more than one plot to present all gathered data, as at least either the temperature or bias voltage stays constant. In the respective diagrams in figure 3.11 the bias voltage is 30 V, but there is usually also data for 25 V, 20 V and 15 V. One exception is the Kapustinsky driver in the fast setting, as it only starts flashing at 16 V, c.f. figure 3.3.

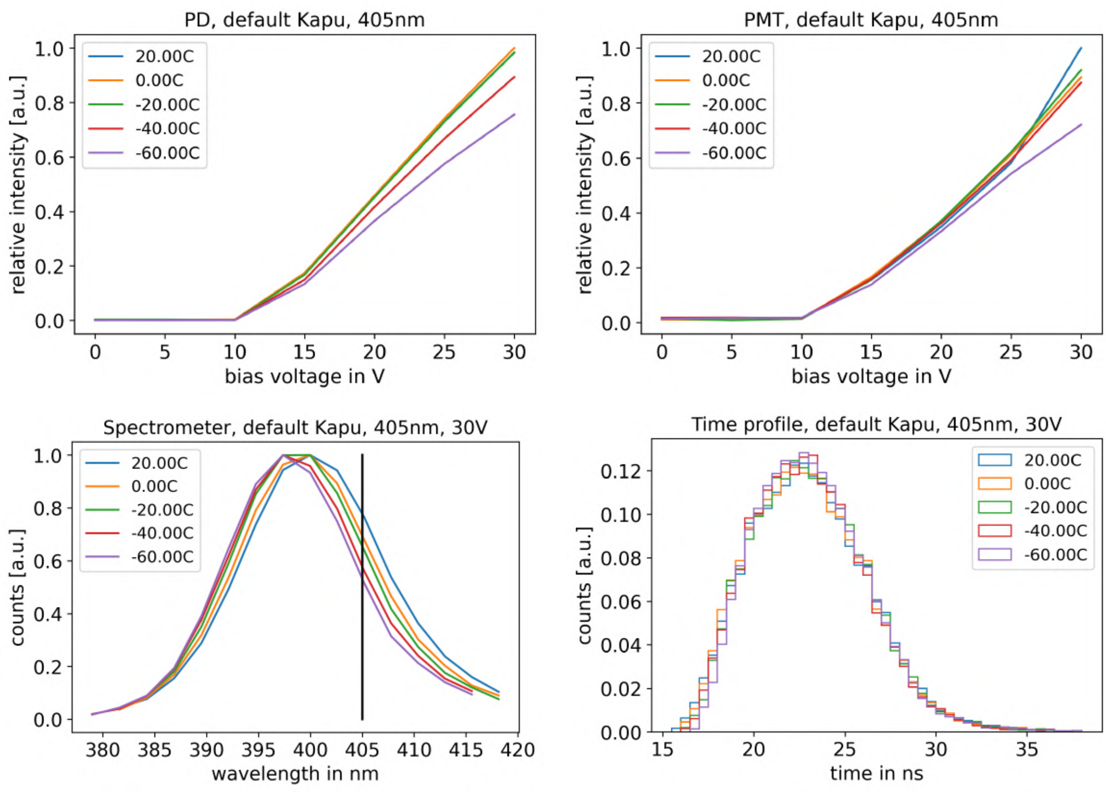

Figure 3.11: Example of usual plots using POCAS data. The relative intensity measured by the PD (top left) and PMT (top right) is plotted in dependence of the bias voltage. For the wavelength spectrum (bottom left) and time profile (bottom right), the bias voltage was 30 V. The black line denotes the nominal wavelength of 405 nm. The same data as in [35] is used in a similar representation.

Chapter 4

Calibration station data analysis

The raw data from the calibration station is given in a h5-file and we can present the measurements in plots like figure 3.11. However, even in the latter case the representation and underlying data still is rather extensive regarding the implementation into the database [40] that is developed for the IceCube Upgrade. As an example, we can use the time profiles where we would have to consider individual histograms for several flashers and diodes at several temperatures and bias voltages. Therefore as goal of this thesis, we want to find and extract quantities to describe the data in an easier way and without losing critical information. The idea is to generate heatmaps where said quantities are displayed in dependence of bias voltage and temperature. Further, we search for linear behaviours that could allow measurements at e.g. less bias voltages. For the final calibrations it is currently planned to vary the freezer temperature in 10 °C steps between $-60\,°C$ and 20 °C and to vary the bias voltage in 5 V steps between 0 V and 30 V [15]. These are the two main quantities that are considered in this thesis. However, the temperature step is 20 °C in the used calibration data. Moreover, we operated the LD-driver in a configuration that did not allow for a manual setting of the *full width at half maximum* (FWHM) in the respective time profiles.

4.1 Intensity

4.1.1 Photodiode

Here, it is clear that the relative intensity can be easily plotted in a heatmap. Essentially, both plots in figure 4.1 include the same information that is needed to characterise the relative intensity for one flasher and diode.

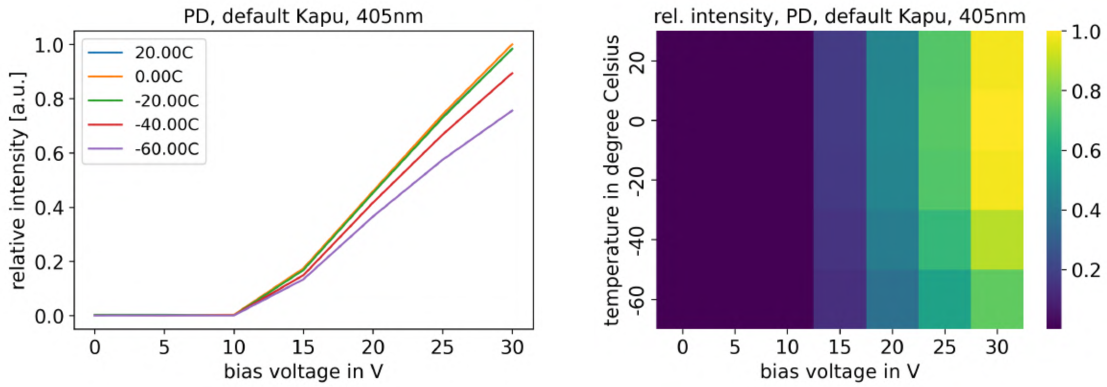

Figure 4.1: Left: Graph for the relative intensity measured by the PD. As example, we show the default Kapustinsky driver and the 405 nm LED. Right: Heatmap of the respective data.

One characteristic of a Kapustinsky circuit is its linear light output with bias voltage [34]. The data for both available 405 nm diodes in figure 3.3 confirms this and also hints that the LD-driver produces a linear response. The plot shows that the fast and default Kapustinsky and the LD-driver start flashing at 16 V, 10 V and 5 V, respectively. Now, we want to further analyse linear behaviours for all flasher configurations. We use the graphs in figures 4.1 and A.4 where most plots show the expected linear response. Only the 365 nm LED will be excluded from the analysis as some necessary modifications in the upstream circuit lead to non-linearities [35]. Other plots also show regions for low relative intensities where the trend does not seem linear. For the fast Kapustinsky driver and the 405 nm LED, this can be likely explained with the resolution of 5 V in our data. Therefore, it does not include the aforementioned starting point.

In table 4.1 we show the gradients of linear fits to the PD data and use the standard deviation estimates as errors. We depict a flasher in one line and then iterate through all five temperatures in the columns. Additionally, we sometimes consider two voltages for one configuration. They refer to the first data point that is included in the fits. Naturally, the standard is to use the highest voltage without intensity as starting point. However, we sometimes exclude this point and begin the fits at the first bias voltage with non-zero intensity. We expect differences in the gradients in both cases, e.g. for the fast Kapustinsky driver and the 405 nm LED. In this example the largest deviations arise and the gradient increases by up to 26%. Therefore, it is necessary to include the right data points when creating the fit.

Table 4.1: Gradients of the linear fits to the PD data for seven out of eight flasher configurations. The first voltage included in the fit can be varied.

	20 °C	**0 °C**	**−20 °C**	**−40 °C**	**−60 °C**
def. Kapu 405 nm					
10 V	0.050±0.002	0.051±0.002	0.051±0.002	0.046±0.002	0.039±0.002
15 V	0.054±0.001	0.055±0.001	0.054±0.001	0.050±0.001	0.041±0.002
fast Kapu 405 nm					
15 V	0.057±0.009	0.060±0.009	0.065±0.009	0.067±0.010	0.066±0.010
20 V	0.072±0.007	0.075±0.006	0.081±0.005	0.083±0.006	0.082±0.004
def. Kapu 465 nm					
10 V	0.050±0.002	0.050±0.001	0.049±0.001	0.046±0.001	0.042±0.001
fast Kapu 465 nm					
10 V	0.049±0.008	0.050±0.005	0.051±0.005	0.051±0.005	0.049±0.004
15 V	0.059±0.004	0.059±0.003	0.059±0.002	0.059±0.002	0.056±0.001
LMG 405 nm					
5 V	0.041±0.001	0.039±0.001	0.038±0.002	0.037±0.002	0.034±0.003
10 V	0.043±0.001	0.041±0.001	0.041±0.001	0.040±0.001	0.039±0.002
LMG 450 nm					
5 V	0.041±0.001	0.035±0.001	0.029±0.001	0.021±0.001	0.013±0.001
LMG 520 nm				(*)	(*)
5 V (*)=10 V	0.037±0.003	0.038±0.003	0.042±0.003	0.052±0.003	0.054±0.005
10 V (*)=15 V	0.037±0.005	0.040±0.004	0.045±0.004	0.051±0.005	0.062±0.004

We can confirm that most plots are linear as expected. In general, it also seems that the fits get better when we exclude one bias voltage, as the respective uncertainties for the gradients get smaller. One special case is the 520 nm LD where the relative intensity at high bias voltages does not drop with temperature as it is expected from the other graphs. We note that it is also possible to plot the intensity at constant bias voltages in dependence of the temperature. Here, we could find further linear behaviours e.g. for the 365 nm LD. However, this analysis is not presented here.

4.1.2 Photomultiplier Tube

The heatmap for the PMT (c.f. figure 4.2) is generated in the same way as the one for the PD. We present no further analysis regarding possible linear behaviours. As already discussed, we mainly use the PD to measure intensities. Further, we have certain regions for each flasher were a non-linear behaviour of the PMT is expected. This can be seen in the respective intensity plots in [15].

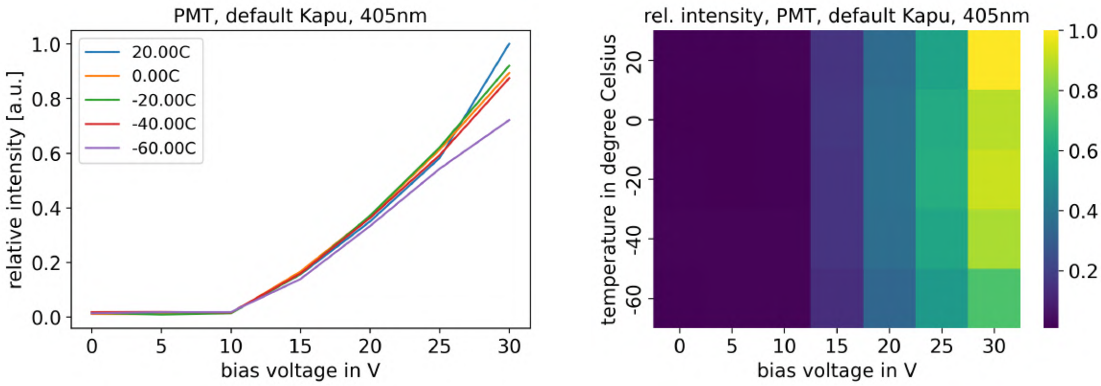

Figure 4.2: Left: Graph for the relative intensity measured by the PMT for the default Kapustinsky driver and the 405 nm LED. Right: Heatmap of the respective data.

4.2 Wavelength

The spectrometer records data for 288 spectral bins and we use a few dozen points to plot a spectrum like figure 3.11. We will try to fit the respective data with a Gaussian curve following formula 4.1, with the amplitude A, mean wavelength μ and standard deviation σ.

$$f(x) = A \cdot \exp\left\{\frac{-(x-\mu)^2}{2\sigma^2}\right\} \tag{4.1}$$

Further, we want to quantify a goodness-of-fit value. It is calculated using the same basic idea as the *least squares*-method, e.g. [41], where we calculate the sum of the squared residuals between n given data points y_i and a fit function $f(x_i)$.

$$LS = \sum_{i=1}^{n} (y_i - f(x_i))^2 \tag{4.2}$$

The LS-value is normally minimised in order to find a linear regression model, but we note that we just calculate LS to quantitatively characterise our Gaussian fits and do not apply the whole method.

The results for all driver and diode combinations is shown in figure 4.3. In each case we considered n=28 data points in the region around the maximum. We depict the mean LS-value considering all recorded temperatures and bias voltages. The respective standard deviations are included as uncertainties. It seems that the use of the fast Kapustinsky driver provides a worse Gaussian spectrum compared to the default case, while the Gaussian shape gets clearer with higher wavelengths for the LMG. An explanation could be that higher absolute intensities lead to higher statistics and a well pronounced Gaussian curve.

We note that the depicted LS-values in figure 4.3 are only relative. To provide a rough scale how they translate absolutely, we show two examples in figure 4.4. The LMG driver and 520 nm LD provide an almost perfect Gaussian spectrum and the used fit is also suitable in the worst case with the fast Kapustinsky driver and the 465 nm LED. The bias voltage and temperature in the examples were arbitrarily chosen and are equal to 30 V and 20 °C.

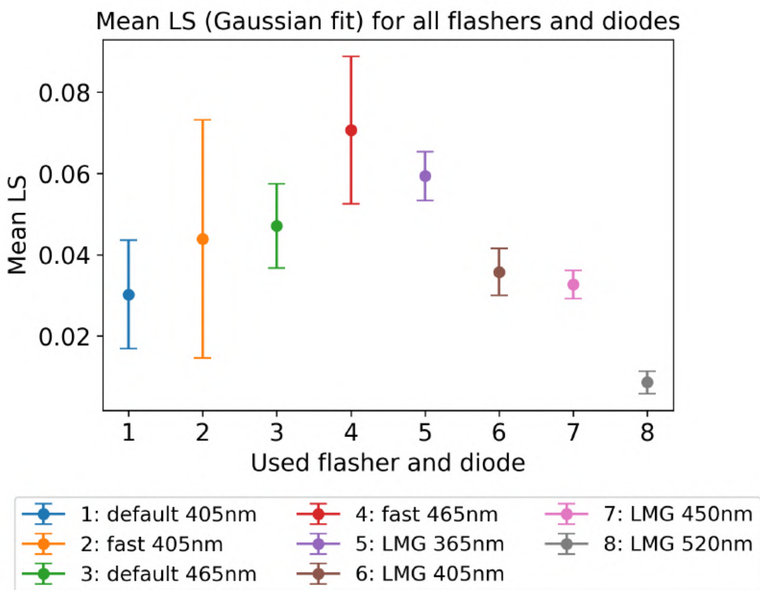

Figure 4.3: Mean LS value and standard deviation for all flashers and diodes. The data from the LMG driver with the 520 nm LD and the fast Kapustinsky driver with the 465 nm LED provide the best and worse Gaussian shape, respectively.

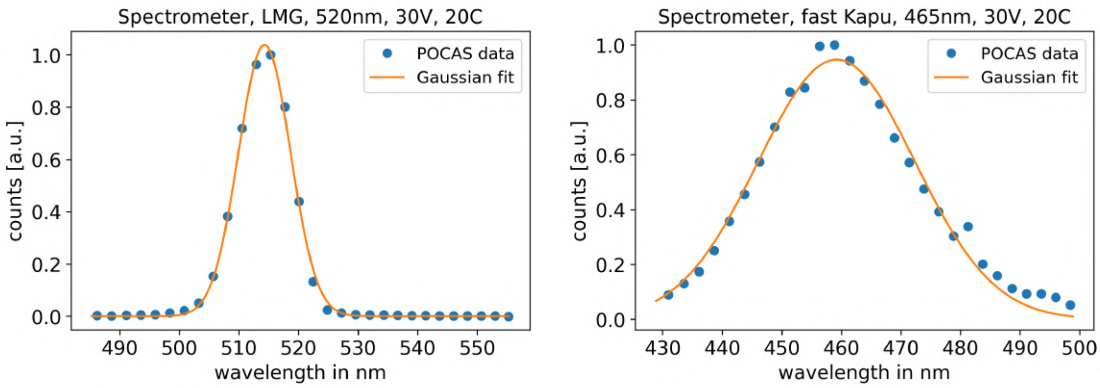

Figure 4.4: Examples at arbitrary bias voltage and temperature for the best and worst fit. Left: Example of a Gaussian fit for the 520 nm LD. Right: Example of a Gaussian fit for the 465 nm LED and the fast Kapustinsky.

Since we use the calibration station for the relative flasher characterisation, A can be neglected in our analysis. We only need to consider μ and σ when applying a Gaussian fit to the recorded data. However, as it is less abstract, we use the FWHM which is equal to $2\sigma\sqrt{2\ln 2}$. This value can be obtained by solving equation 4.1. Both said quantities that now fully represent the recorded spectra are shown in heatmaps in figure 4.5. For the wavelength measurement, we reduced the number of needed data entries for the IceCube Upgrade database by roughly one order of magnitude.

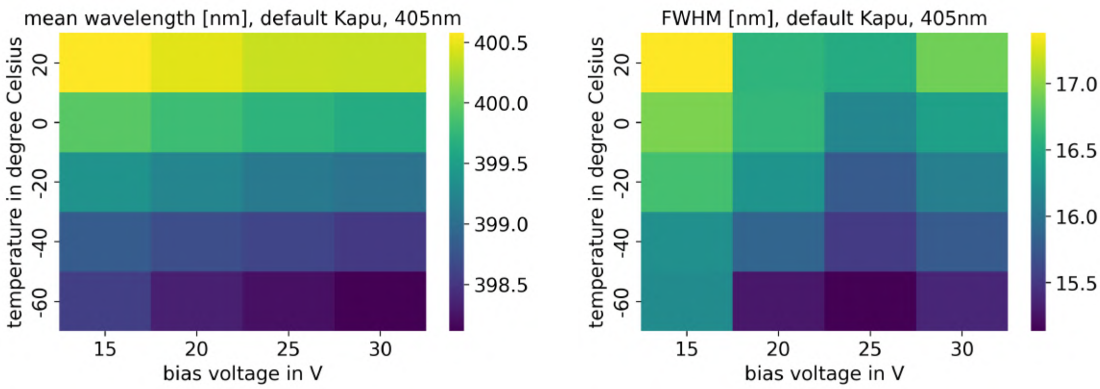

Figure 4.5: Left: Heatmap for the mean wavelength of the Gaussian fit to the spectrometer data. Right: Heatmap for the FWHM of the Gaussian fit to the spectrometer data.

The mean wavelength and FWHM can now be plotted similarly to the relative intensities. Again, we choose to represent the data for constant temperatures in dependence of the applied bias voltage. After all, the latter is the quantity that can varied during the POCAM application at the South Pole. It was already observed that the mean emission wavelength can decrease with bias voltage considering a default Kapustinsky flasher [29]. We want to extend this observation to the FWHM and all flasher configurations.

We show the plot for the default Kapustinsky driver with the 405 nm LED in figure 4.6. For all temperatures the mean wavelength drops slightly and a linear dependence is visible. The difference to the nominal wavelength is larger than in [29], but the gradient is consistent. The change in the FWHM is similar for all temperatures, but harder to interpret and no references for comparison exist. Our recorded spectrometer data has a resolution of roughly 2.7 nm and the question arises if the changes in the FWHM have a physical background. We speculate that maybe a lower temperature leads to less phonons in the semiconductor and consequently to more pronounced emission wavelengths and a smaller FWHM. Its behaviour for the remaining Kapustinsky flashers in figure A.5 is also not conclusive, especially in the fast setting. Only for the default and 465 nm case the FWHM increases 3 to 4 nm and similarly for all temperatures. For the mean wavelengths we notice roughly linear responses in all plots. However, the absolute differences for the 405 nm LED are apparently smaller and contrary to the other LED it shows no clear decline with the bias voltage.

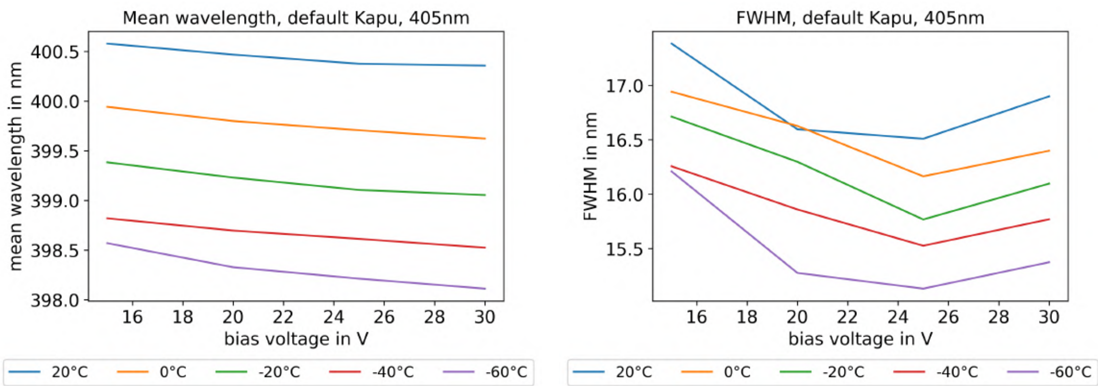

Figure 4.6: Mean emission wavelength (left) and FWHM (right) of the Gaussian fit for the default Kapustinsky driver and the 405 nm LED.

For the LMG circuit we start exemplary with the 405 nm LD in figure 4.7. At all temperatures the mean wavelength increases linearly and approximately 1 nm in total.

For the FWHM we can see no consistent behaviour, but the changes are not significant in their relative and absolute magnitude. The remaining LMG-driven diodes are shown in figure A.6 and the 450 nm LD shows an almost similar behaviour to the previous example. The mean wavelength for the 365 nm LED stays more or less constant with only small deviations and a tiny increase. This behaviour is also given for its FWHM and it is the only respective plot where we see a clean ordering with temperature. Considering the 520 nm LD the decrease of the mean wavelength seems linear at higher temperatures, but becomes smaller and non-linear at lower temperatures. The general increase in the FWHM is too small to be conclusive.

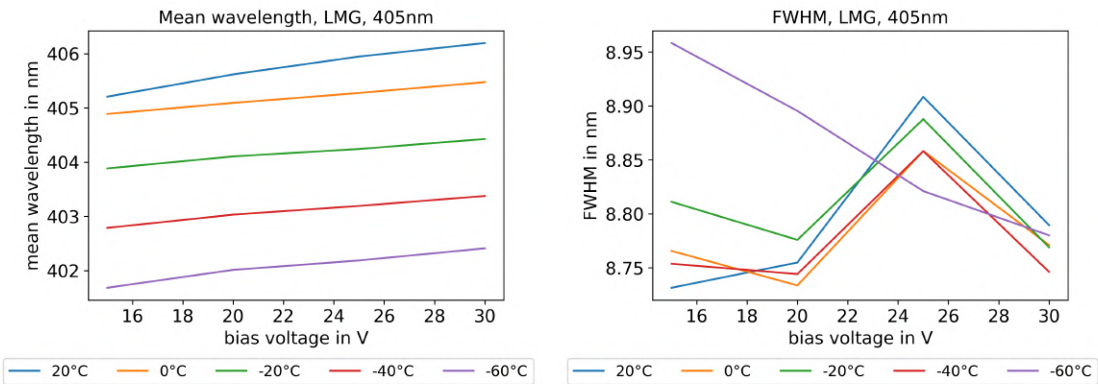

Figure 4.7: Mean emission wavelength (left) and FWHM (right) of the Gaussian fit for the LMG driver and the 405 nm LD.

4.3 Time profile

The time profiles from the Avalanche Photodiode (APD) form the most sophisticated analysis in this thesis. Unlike with the intensity measurement, there is no obvious quantity that can be extracted and plotted in heatmaps. It is also not possible to describe all profiles with a common function e.g. a Gaussian curve. Exemplary, we show the histograms in figure 3.11 and the two examples in figure 4.8. In [35] the time profiles for all remaining flashers and diodes can be found. An analysis regarding linear behaviours in the time profiles is not expedient and and will be disregarded.

The basic idea to describe the time profiles using less data than the histograms is to follow the respective shapes with multiple linear fits. For this we need to determine certain pairs of (x, y) or (time, counts) where a line with a certain gradient begins or ends. To find these points we use two different methods. The first one defines volume levels and the second method uses height levels. In both cases, we then search for the bin where we find e.g. 25% and 50% of the histogram's volume or height, respectively. This process leaves us with a certain number of (time, count)-pairs that can then be depicted in heatmaps. In the following chapters we will briefly explain both methods and then compare them to choose the better technique.

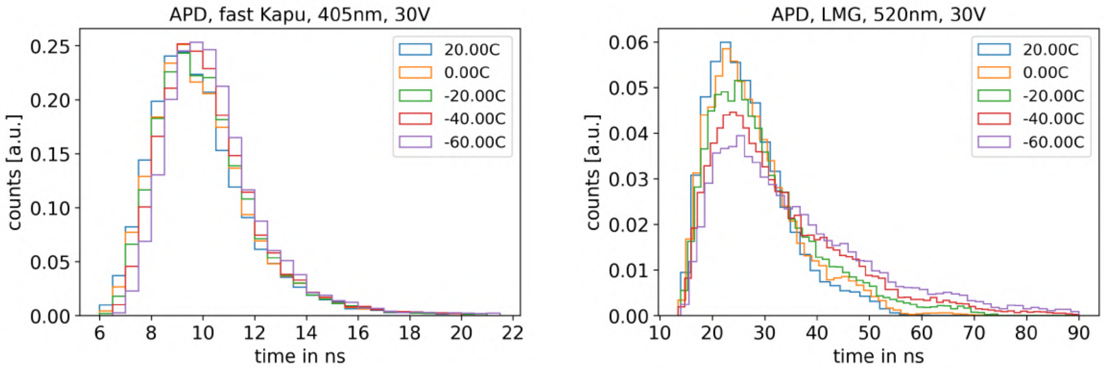

Figure 4.8: Left: Time profile of the fast Kapustinsky driver with the 405 nm LED at 30 V bias voltage. Right: Time profile for the LMG driver and the 520 nm LD at 30 V bias voltage. This flasher produces the longest tails.

4.3.1 Method 1: Volume levels

For this method we define volume levels where the histogram's volume is interpreted as the sum of all counts. How the profile is then recreated is illustrated in figure 4.9. On the left side we show black lines where a respective volume percentile is located. As fit point we choose the middle of the bin where a line is located. These points are then connected to form the recreated profile. At the beginning and end of the profile we set the fit points to zero and empirically 0.002 and 0.999, respectively, have been chosen as levels for all histograms. We note that these two values are always included, even if they are not specifically mentioned.

The levels in the example are [0.2, 0.4, 0.6, 0.8, 0.9, 0.95, 0.99] resulting in nine total points. We can already make observations regarding the rough position of certain levels. The peak is located slightly above 40% and we have to include levels between 95% and 99% to correctly represent the tail. Around the peak and before the tail we have the highest curvatures and generally expect more points there in a better fit. Moreover, in the depicted profile the whole rising edge can be described with one line. For this specific example, we show some of the corresponding heatmaps in figures A.7 and A.8.

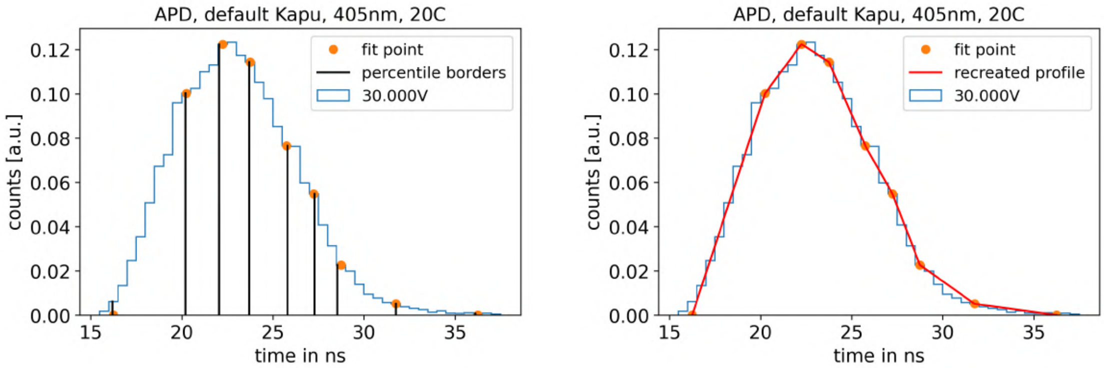

Figure 4.9: Process to recreate the time profile of the 405 nm LED and the default Kapustinsky driver with the first method using volume levels. The temperature and bias voltage equal 20 °C and 30 V, respectively.

4.3.2 Method 2: Height levels

Here, the height of a histogram is determined by its highest count and the horizontal levels are given as proportions of this value. They are depicted as black lines in figure 4.10 where the technique is shown. We define one fit point as the middle of the first bin that has a higher count than a certain level. As the histogram also crosses the same level on the falling edge, we then also include the first lower bin as a point. There are two exceptions to this approach, with the first one being the starting and endpoint of a fit. Their corresponding bins are determined as described before, but the corresponding y-values are automatically put to zero. Typically, we use 1% or 0.5% as a low level. Additionally, we always include one point with a larger count than 99% of the height. This is usually, but not necessarily, the peak. In total, we only get an uneven number of fit points with this method.

The fit in figure 4.10 was created with levels of [0.15, 0.3, 0.5, 0.8] resulting in 11 points including the beginning, peak and end of the profile. The general position of a level is clearer than in the first method, but we can also make further deductions. Due to its shape, a small change of a level in the tail region can result in a rather large change in the x-value of the corresponding fit point. Additionally, we observe that this method could produce unnecessary points, e.g. on the rising edge.

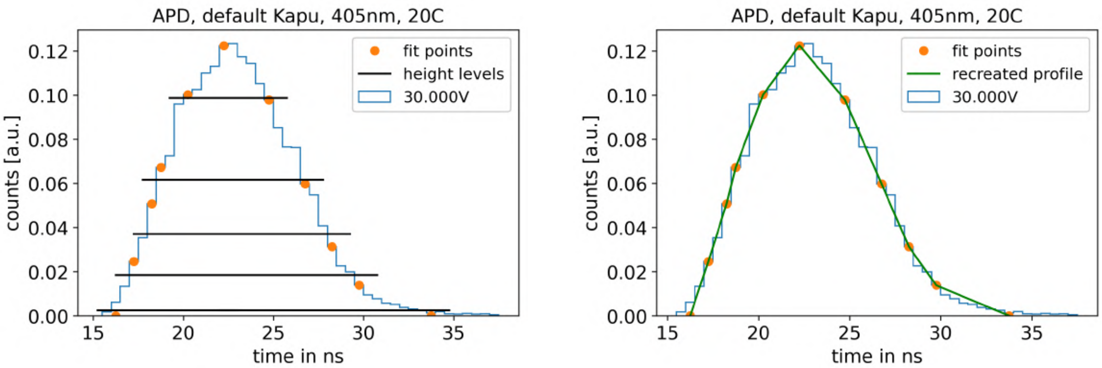

Figure 4.10: Process to recreate the time profile of the 405 nm LED and the default Kapustinsky driver with the second method using height levels. The temperature and bias voltage equal 20 °C and 30 V, respectively.

4.3.3 Comparison of both methods

Here, we compare both methods for a given number of levels. In the end, we want to determine the better method and ideally a suitable number of levels or rather data points. At some point we expect that an increasing of both only leads to a small improvement of the fit. In the comparison we calculate the LS-value from equation 4.2 for both fits and individually for every flasher and diode. Regions with counts, but without fit are also considered. Again, we take the average over all temperatures and bias voltages and use the standard deviation as an error. We note that we introduce an unknown weighting with this approach, as not all histograms have the same number of bins. However, we do not consider this effect further and it is included in the errorbars.

The essence now lies in identifying the levels that provide the best fits. This is done by calculating the mean LS-value for a certain number of random levels in the order of 10^3. We then choose the levels that provide the smallest LS-value. We note that this approach does not necessarily return the global minimum for each histogram and the respective number of data points. However, this is the case for both methods and we assume that this technique is valid to determine which method generally provides the better fit.

To generate the random levels we use the *numpy.random.uniform* function [42] in Python. Per default it returns numbers between zero and one and each value is equally likely. We can also include the two parameters *low* and *high* and the returned value will be in the half-open interval [*low*, *high*). This can be used in some extent to favour levels that are already known to be suitable. In equation 4.3 we show a typical example for the levels [x_1, ..., x_n] in method 1.

$$x_1 = [0.003,\ 0.5), ...,\ x_{n-1} = [x_{n-2},\ 0.95), x_n = [x_{n-1},\ 0.999) \tag{4.3}$$

At ≥ 7 total levels we also permanently introduce a level in the interval [0.98, 0.998) and subsequently change the high value in x_n to 0.98. For the second method, we use a similar structure, but favour low levels by putting relatively small upper bounds. Here, we also always include a low level (< 0.15) for ≥ 7 total fit points.

For all eight flasher configurations, we then produce a plot like figure 4.11 where we can usually already deduce a preferred method. As the LS value is only a relative quantity, we need to show exemplary profiles. For simplification we will use 11 as the default number of fit points and always show an example for both methods. A recommendation for the amount of fit points is then done after a visual assessment of the chosen method. We note here that the decision may also rely on diagrams that are not shown in this thesis. It would be too extensive to include all plots that are taken into account. When we show an example for both techniques, we naturally need to select the same temperature and bias voltage. For this we search a profile where both LS-values are as close as possible to their respective mean.

Figure 4.11 compares the mean LS-values for the 405 nm LED and the default Kapustinsky driver. As expected, the fits get better with a higher number of points, but their absolute improvement decreases. For a low number of points, method 1 is better, but at higher numbers method 2 returns the slightly smaller LS-values. At some point the main differences between fit and histogram arise in the region around the peak and the tail. In the former, it can happen that the fits cut through the histogram, as method 1 does not automatically include the peak and method 2 cannot catch high plateaus, local minima on the rising edge and local maxima on the falling edge. In the tail region the main problem is that the fit can be above the histogram. As we increase our number of fit points, these two problems get reduced. In figure 4.12 we show two examples and our recommendation would be method 2 with 11 points. We note that it is usually possible to choose a higher number of points without further assessment, but we try to make a trade-off to select the smaller number and the size of the errorbars is also considered.

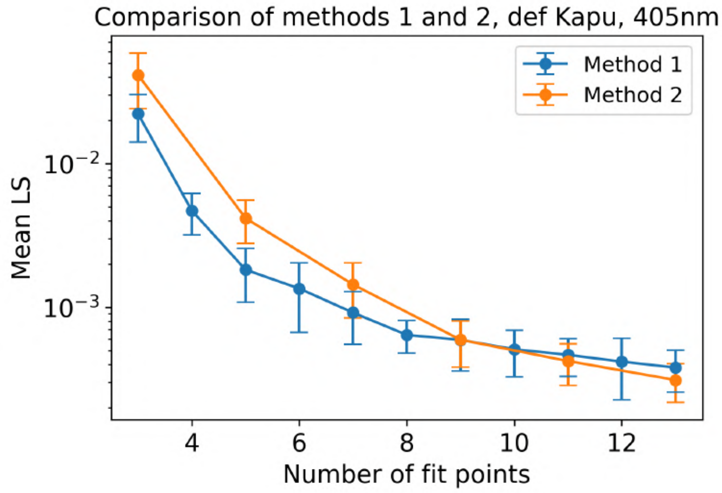

Figure 4.11: Comparison of both methods for the default Kapustinsky flasher and the 405 nm LED. Method 2 is worse in the beginning, but seems to produce the slightly better fit for 11 and 13 points.

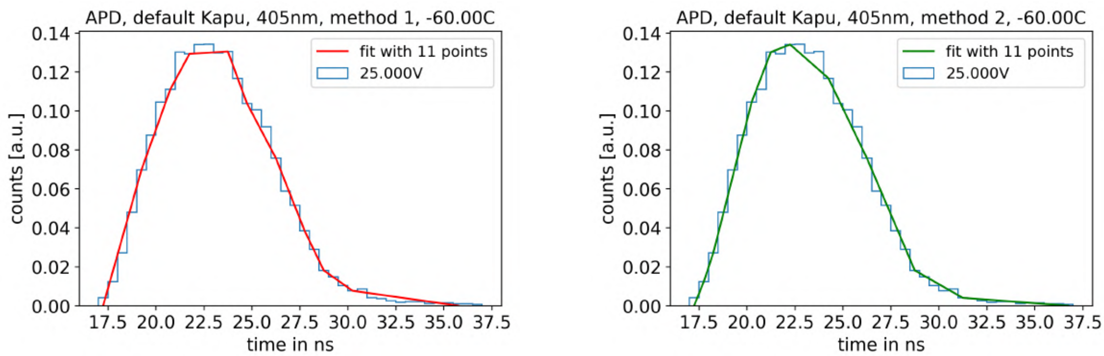

Figure 4.12: Two exemplary fits for the default Kapustinsky driver with the 405 nm LED. Method 1 is on the left and method 2 on the right. The largest deviations between both fits and the histogram are around the peak.

The next case is the fast Kapustinsky flasher with the 405 nm LED in figure 4.13. The main difference to the default setting is that both methods converge after eight points. The next criteria is the standard deviation and we therefore prefer method 1. We show two average examples in figure 4.14 where the main difference is at the peak. It is not included in method 1, but still both fits have almost the same LS-value. However, 11 points are still enough for the first method if we take the remaining histograms into account.

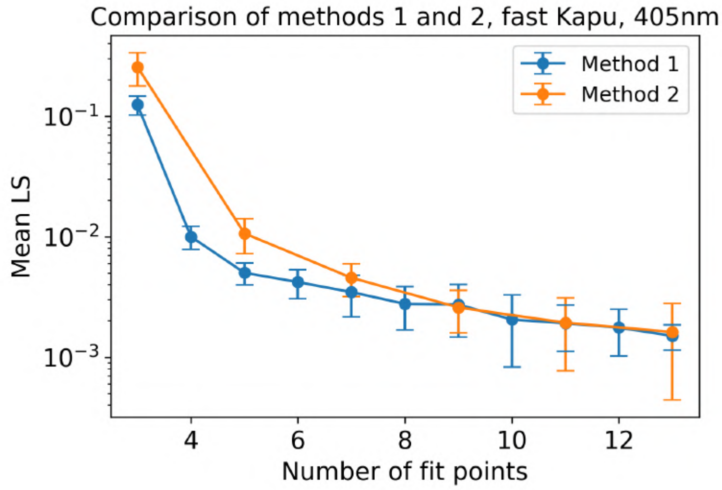

Figure 4.13: Comparison of both methods for the fast Kapustinsky flasher and the 405 nm LED. For a high number of points, there are almost no differences in the mean LS-value.

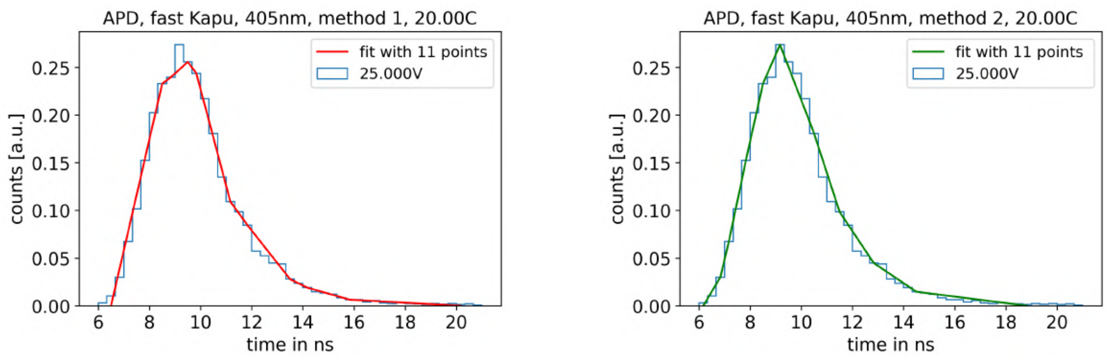

Figure 4.14: Two exemplary fits for the default Kapustinsky driver with the 405 nm LED. Method 1 is on the left and method 2 on the right. The latter does include the peak, but still both fits are similar regarding their LS-value.

In figure 4.15 we show the result for the default Kapustinsky driver with the 465 nm LED. Almost across the whole analysed range, we can see that method 1 provides a better fit and we choose to favour this technique. Additionally, it has smaller errorbars in the region of interest. Two examples are shown in figure 4.16. At all other temperatures and bias voltages the peak is also similar to a plateau and this explains why method 2 is worse. However, we may also need 12 points to describe the profiles properly with method 1.

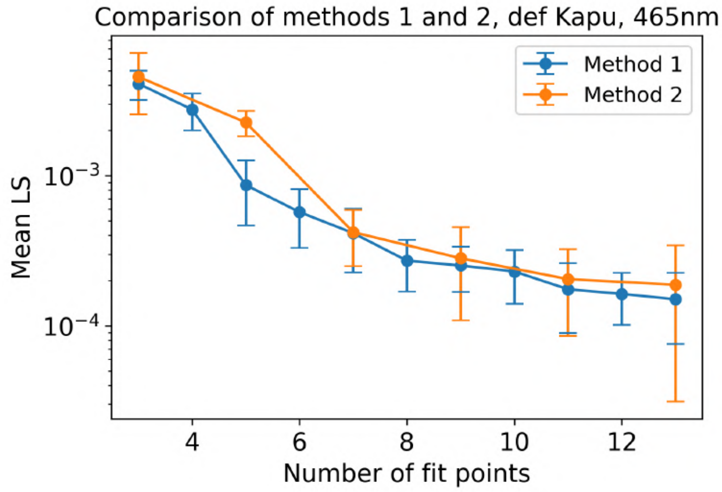

Figure 4.15: Comparison of both methods for the default Kapustinsky flasher and the 465 nm LED. Method 1 provides the better fits for this configuration.

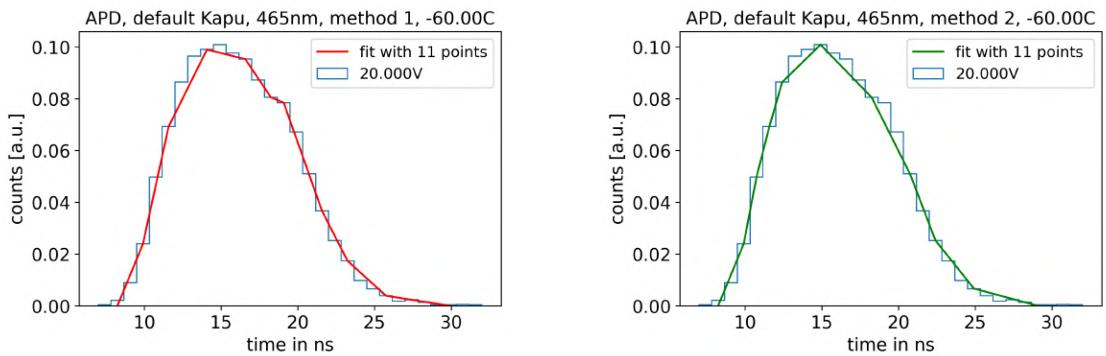

Figure 4.16: Two exemplary fits for the default Kapustinsky driver with the 465 nm LED. The histograms do not have a sharp peak and method 1 is smoother on the falling edge.

The fast setting with the 465 nm LED is the last case for the Kapustinsky driver. We see that the respective plot in figure 4.17 is qualitatively similar to the 405 nm LED. The mean LS-values converge, but the standard deviation for method 2 is higher. In figure 4.18 both fits have exactly the same LS-value and are close to the histogram. However, the other profiles that are not shown indicate that 10 points may not suffice.

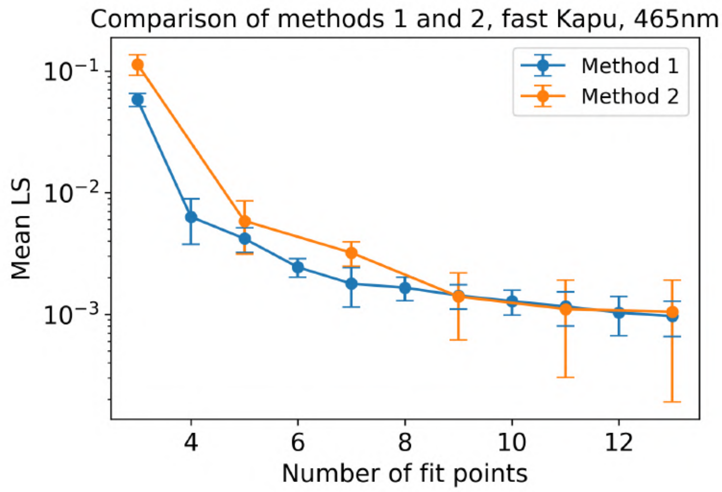

Figure 4.17: Comparison of both methods for the fast Kapustinsky flasher and the 465 nm LED. The graph is similar to the respective case for the 405 nm LED.

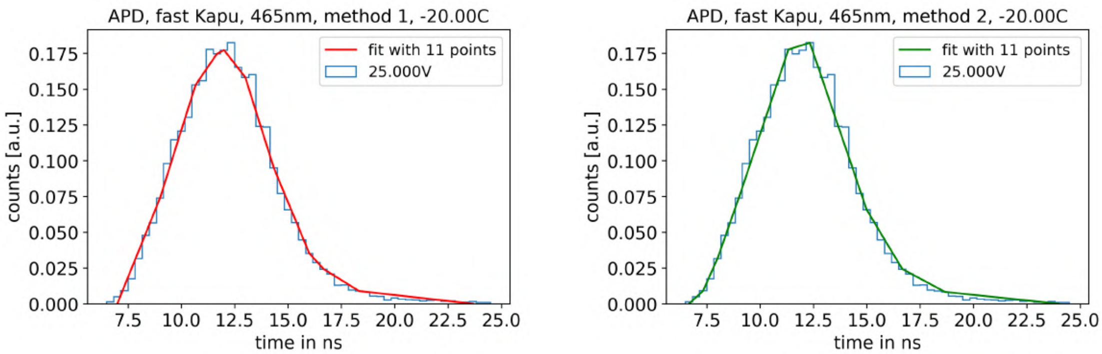

Figure 4.18: Two exemplary fits for the fast Kapustinsky driver with the 465 nm LED. The recreated profiles are almost similar.

The 365 nm LED is the first case for the LMG driver and shown in figure 4.19. The diagram looks similar to figure 4.11. At a high number of fit points method 2 is better, but shows larger uncertainties. However, they are still competitive compared to method 1 regarding their extension to higher LS-values. The two examples in figure 4.20 show that 11 fit points are suitable to recreate the histograms. We note that a simplification to 10 levels would also provide suitable fits, but then we would be bound to method 1.

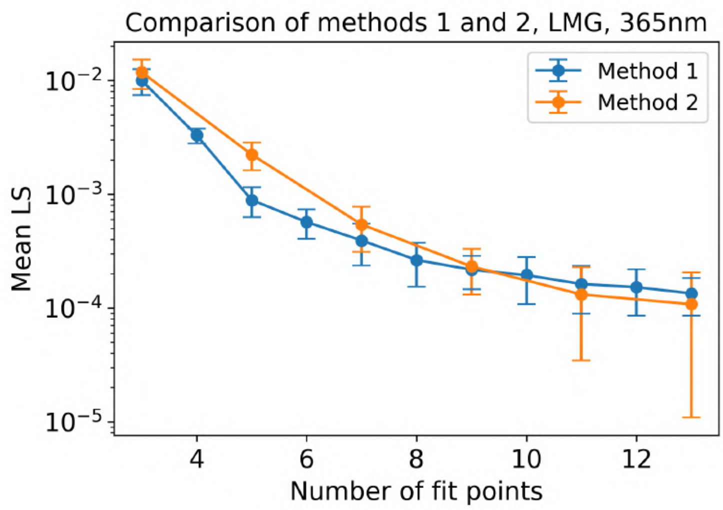

Figure 4.19: Comparison of both methods for the LMG flasher and the 365 nm LED. The graph shows qualitative similarities with figure 4.11.

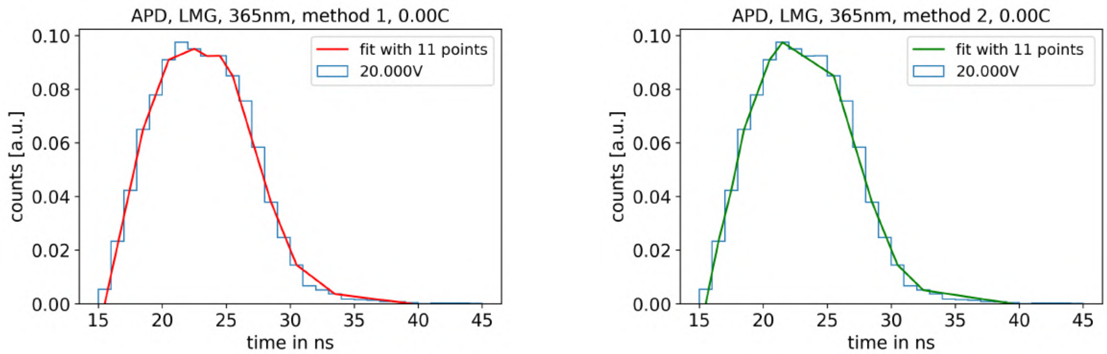

Figure 4.20: Two exemplary fits for the LMG driver with the 365 nm LED. Both recreated profiles are similar, but method 2 has a slightly better LS-value.

The first thing that we notice in figure 4.21 for the 405 nm LD is the large error for method 2 with three fit points. This is caused by one histogram with a relatively high LS-value. It leads to a standard deviation that is larger than the mean. However, we notice that this happens only once. At first both methods are equally suitable, but later method 2 produces better fits with smaller errors. For this flasher configuration, we want to avoid method 1 due to the larger standard deviations. For method 2 all bias voltages and temperatures produce similar results like the good fit in figure 4.22. In most histograms it would also be possible to use the technique with nine points.

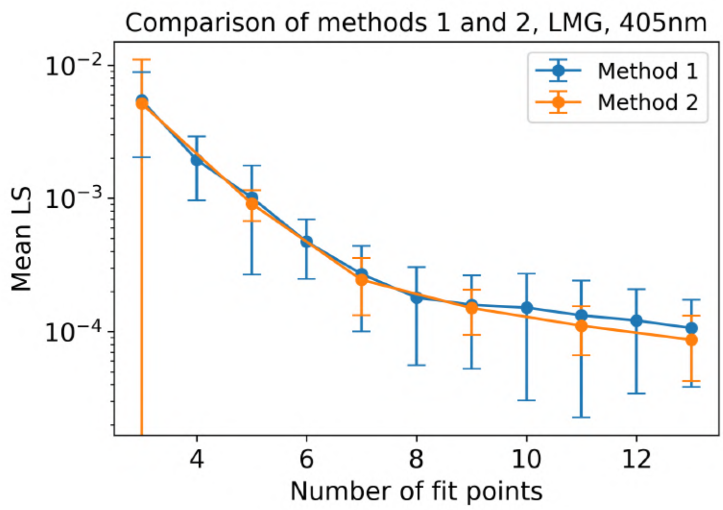

Figure 4.21: Comparison of both methods for the LMG flasher and the 405 nm LD. At first both techniques are equal, but later method 2 gets better and also shows smaller uncertainties.

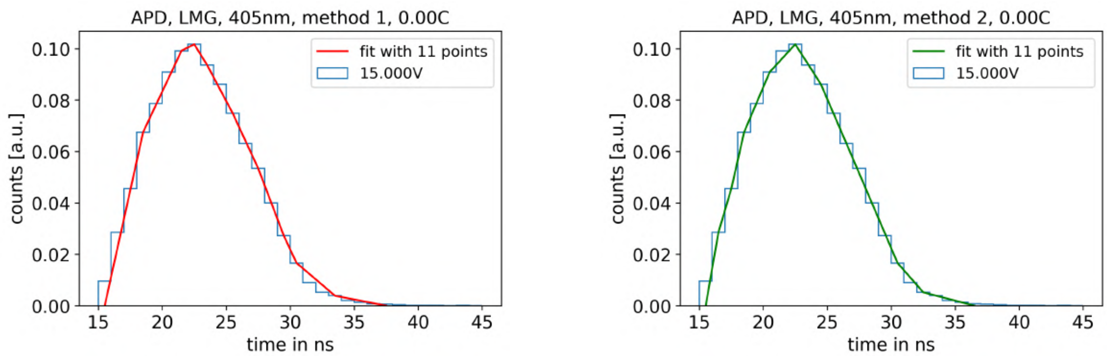

Figure 4.22: Two exemplary fits for the LMG driver with the 405 nm LD. Method 1 provides a higher LS-value, but is also a good representation of the histogram.

Figure 4.23 shows that method 2 is the clear choice for the 450 nm LD. The likely reason for this can be found in figure 4.24. Both techniques produce a similar fit across the whole profile except for the tail. Apparently, the proportion of counts in the tail is so small that it could not be properly resolved with the approach that was mentioned before, c.f. equation 4.3. While the effect is rather extreme in the depicted example, it is still generally less pronounced in method 2. A fit with a lower number than 11 points is not recommended.

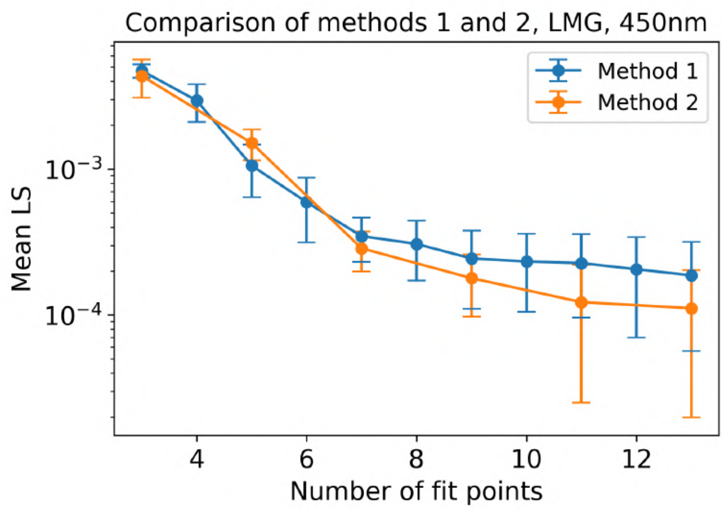

Figure 4.23: Comparison of both methods for the LMG flasher and the 450 nm LD. Method 2 is preferred to recreate the respective profiles.

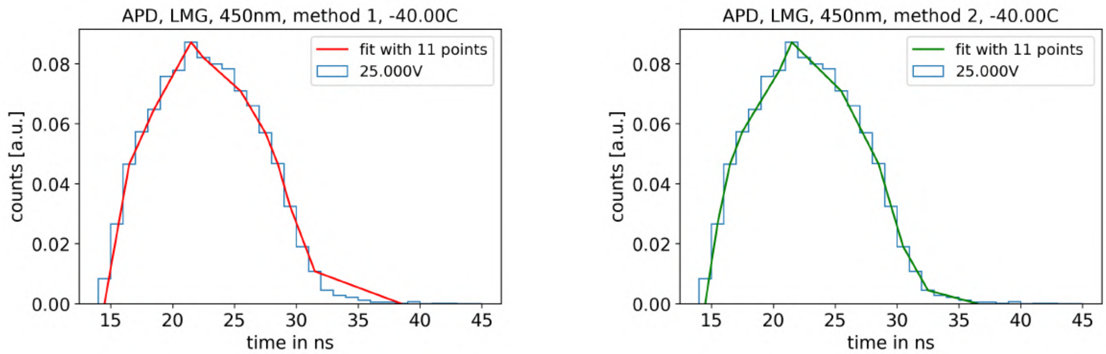

Figure 4.24: Two exemplary fits for the LMG driver with the 450 nm LD. Method 1 does not represent the tail correctly, but otherwise both methods are similar.

The last case is the LMG driver with the 520 nm LD. The respective diagram 4.25 clearly favours method 2, but we encountered some problems regarding its applicability. At nine points it was only possible to find working levels for four out of five temperatures. For the next points this number decreased to two and then zero. The problem is the sharp rising edge in the profiles like figure 4.26. The used code does not work if the expected number of fit points cannot be assigned to different bins. Until this issue is fixed we need to use method 1 or method 2 with only seven fit points. The latter would theoretically be suitable, but we recommend to reach a higher precision.

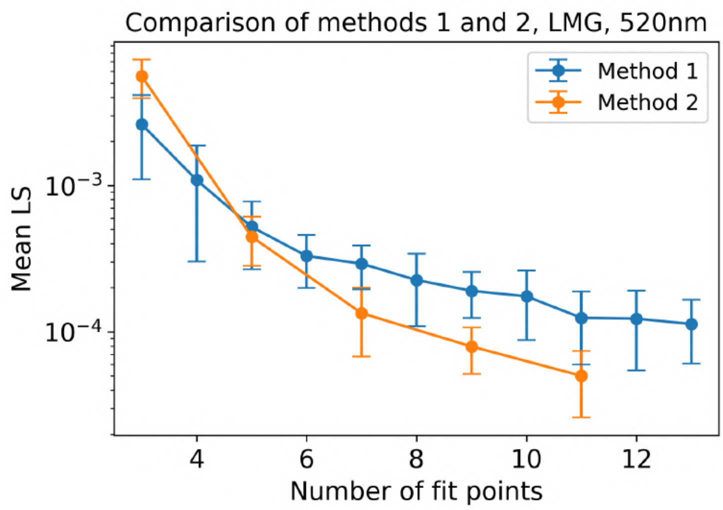

Figure 4.25: Comparison of both methods for the LMG flasher and the 520 nm LD. Method 2 provides the better fit, but does not work properly starting at nine levels.

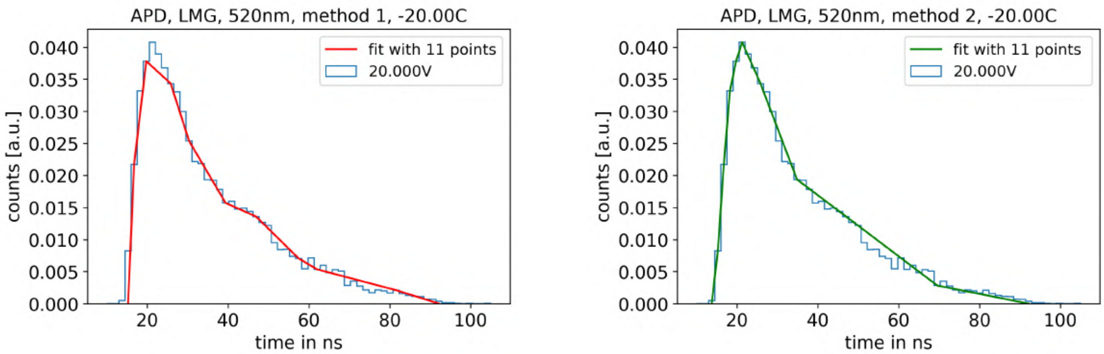

Figure 4.26: Two exemplary fits for the LMG driver with the 520 nm LD. The profile looks very different compared to all other drivers and diodes. The sharp rising edge is clearly visible.

Chapter 5

Summary

The main goal of this thesis was to find ways to transform data from the POCAM calibration station to ease the implementation into the database that is developed for the IceCube Upgrade. To do this, we searched for quantities that can be easily represented in dependence of two parameters, namely bias voltage and temperature. It is then possible to show these quantities in heatmaps. Further, we looked for possible linear behaviours that would allow to conduct less calibration measurements. The thesis is structured in accordance with the three types of analyses that are done by the calibration station. It characterises the relative intensity, wavelength spectrum and time profile of eight different driver and diode combinations that can be flashed by the POCAM.

Normally, the relative intensity is already plotted in dependence of temperature and bias voltage. In the corresponding chapter for the Photodiode as the main instrument, we therefore concentrated on quantifying linear responses. For the Kapustinsky drivers they were expected and largely confirmed. However, it is necessary to correctly determine the bias voltage where a certain driver starts flashing. This cannot always be done with the 5 V resolution in the used data. For the LMG-driven diodes we could also identify clear linear behaviours, especially for the 405 nm and 450 nm LDs.

For the wavelength spectrum, we showed that the recorded data can be fitted with a Gaussian curve. This allowed us to describe the spectrum with the mean wavelength and the FWHM of the fits. These two quantities can then be plotted in dependence of bias voltage and temperature. We observed that the shifts of the mean wavelengths is linear in most cases. The behaviour of the FWHM is more abstract and sometimes erratic. In some cases it can be disregarded and we would then be able to measure the spectrum at less bias voltages without losing critical information.

The transformation of the recorded time profiles was the most complicated analysis in this thesis. We recreate them using multiple linear fits. The coordinates where one line ends and another one begins can then be put in heatmaps. To determine a fit for one specific profile, we use two methods that use levels with respect to the sum of all counts and the histogram's height, respectively. For both techniques we quantify a goodness-of-fit value based on the least-squares method. The best fit is then approximated after simulating a certain number of random levels. Finally, we are able to compare both fits in dependence of the number of points for all flasher configurations. Usually, we can describe the profiles sufficiently with 11 points, but it is not possible to provide a general recommendation for one method. Furthermore, one approach does not work properly for the 520 nm LD. However, we still obtained useful insights for future reconstructions. We now know the advantages and disadvantages of both techniques and know for which flashers and profiles they work best.

Appendix A

Figures

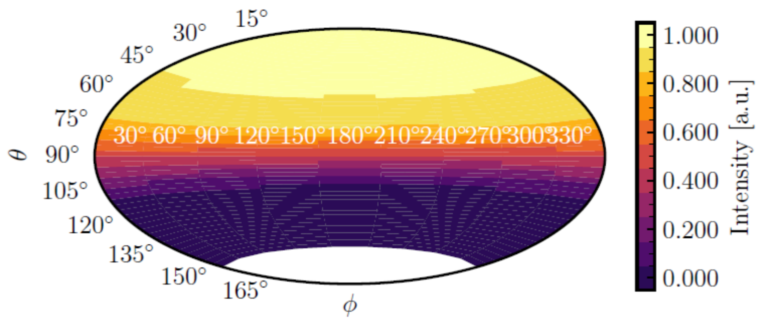

(a) Single hemisphere prototype emission

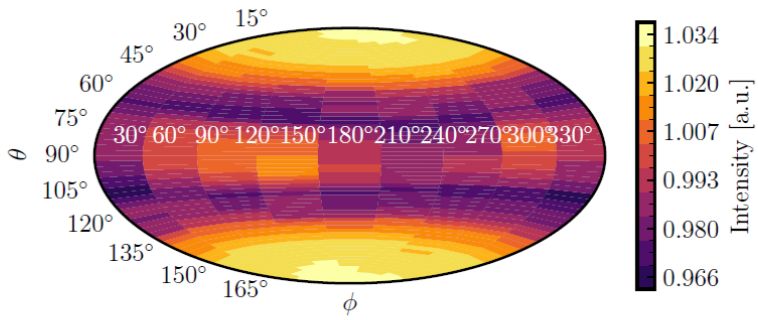

(b) Virtual dual-hemisphere emission

Figure A.1: Measured emission profile for one hemisphere in dependence of zenith and azimuth angle (a) and the virtual sum for two hemispheres (b). Figure taken from [34].

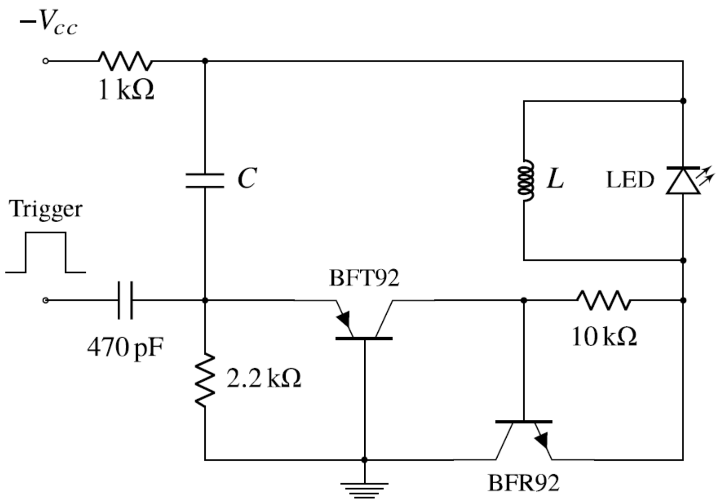

Figure A.2: Schematic view of a Kapustinsky driver. The variation of the capacitor C, the inductance L and the used LED mainly shape the general emission profile. The the circuit can be run with an adjustable bias voltage V_{CC}. Figure taken from [34].

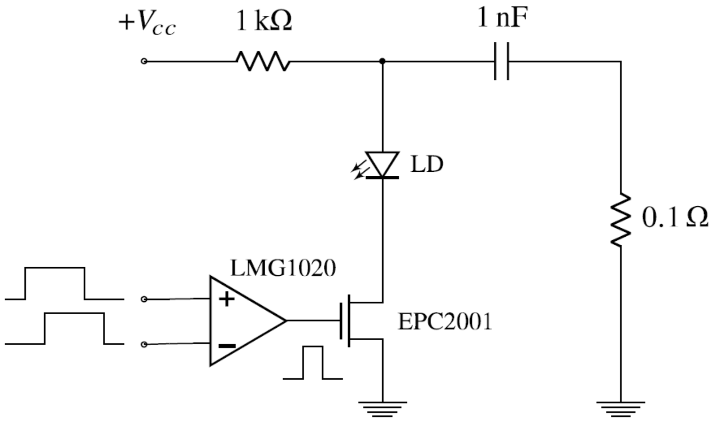

Figure A.3: Schematic view of a LD driver. The trigger pulse, the chosen LD and the bias voltage V_{CC} mainly shape the emission profile. Figure taken from [34].

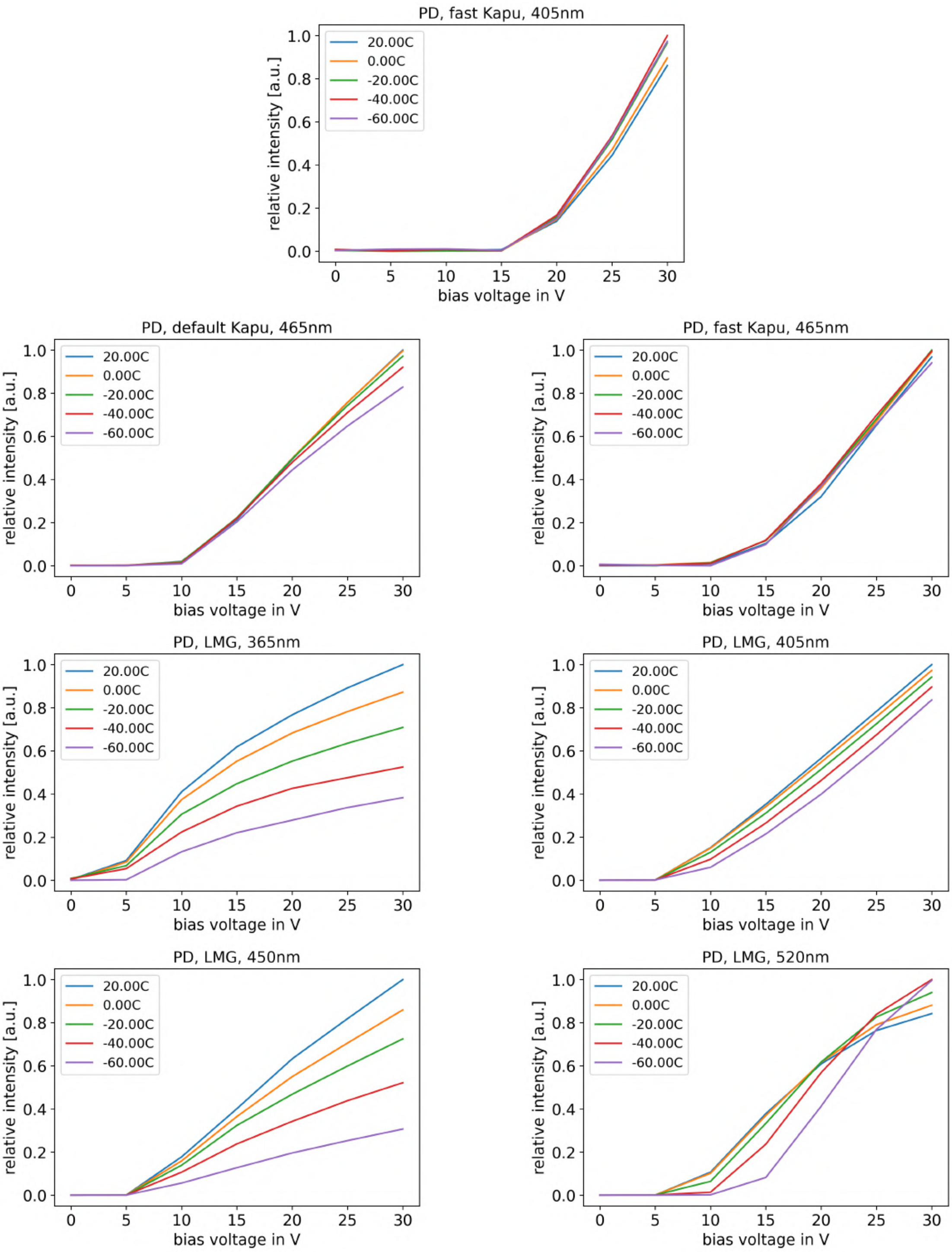

Figure A.4: Relative intensity measured by the PD for all flashers and diodes. The default Kapustinsky driver with the 405 nm LED that is already shown in chapter 4.1.

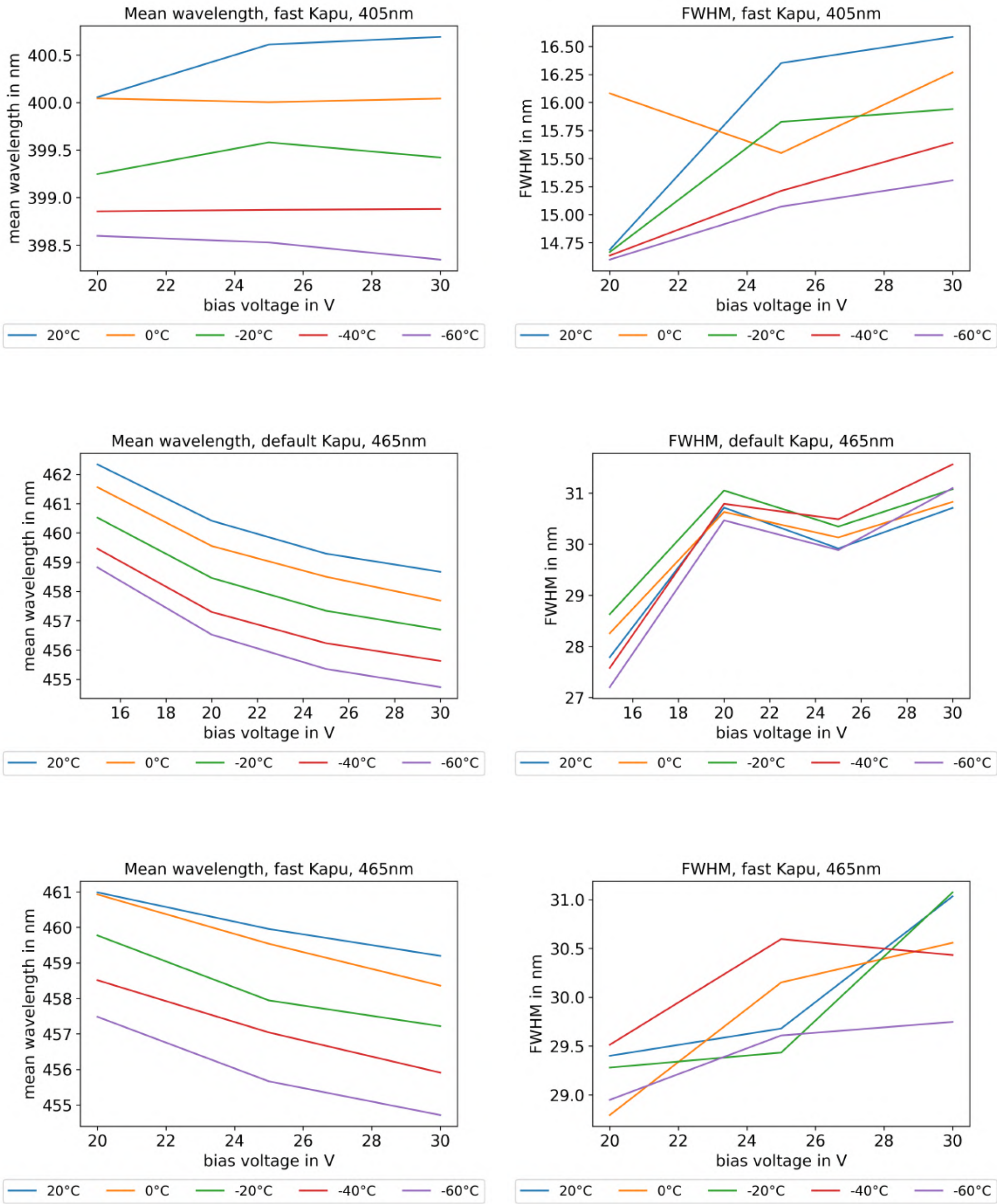

Figure A.5: Mean emission wavelength (left) and FWHM (right) of the Gaussian fit for the remaining Kapustinsky flashers. Top: Fast setting and 405 nm LED. Middle: Default setting and 465 nm LED. Bottom: Fast setting and 465 nm LED.

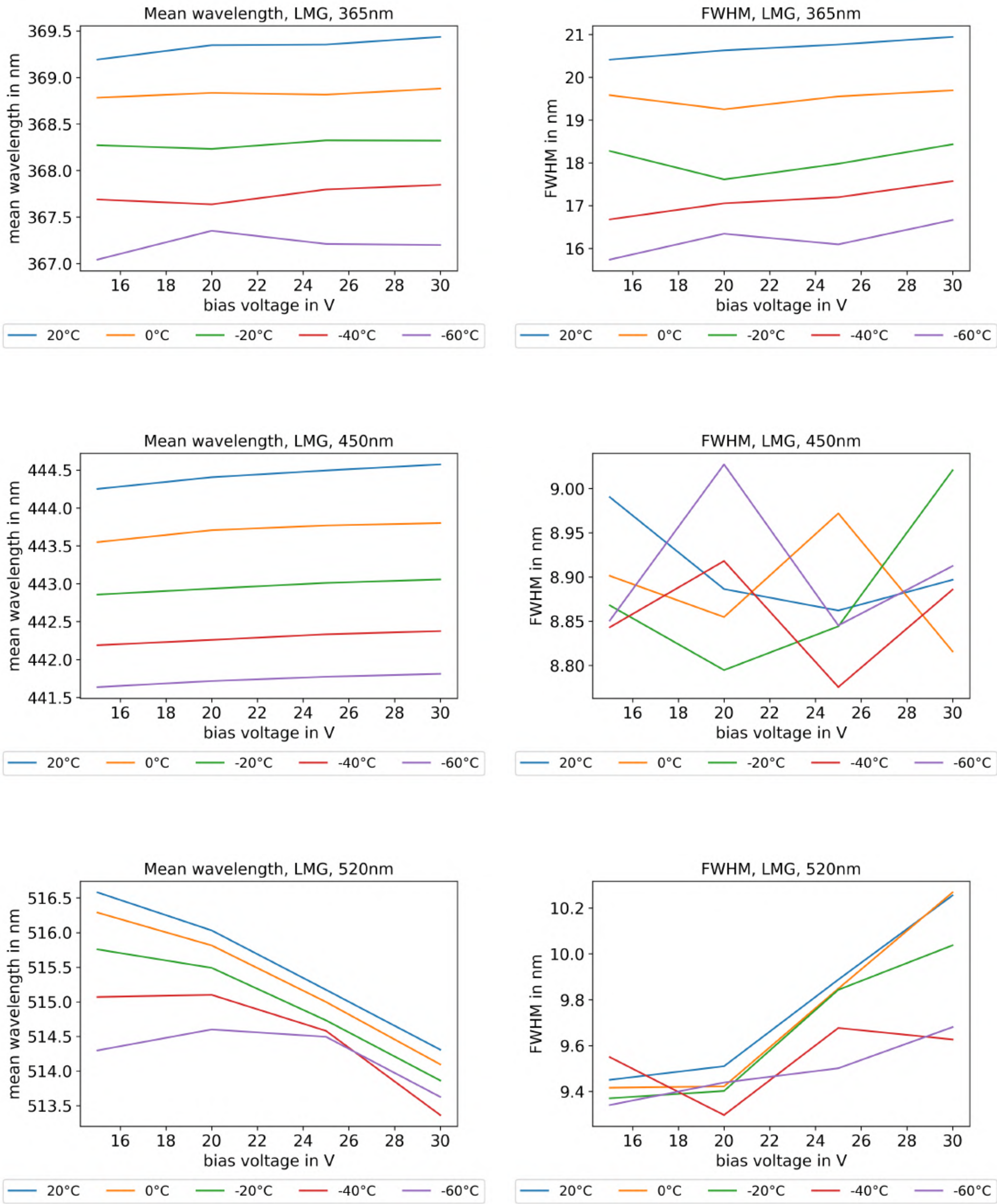

Figure A.6: Mean emission wavelength (left) and FWHM (right) of the Gaussian fit for the remaining LMG flashers. Top: 365 nm LED. Middle: 450 nm LD. Bottom: 520 nm LD.

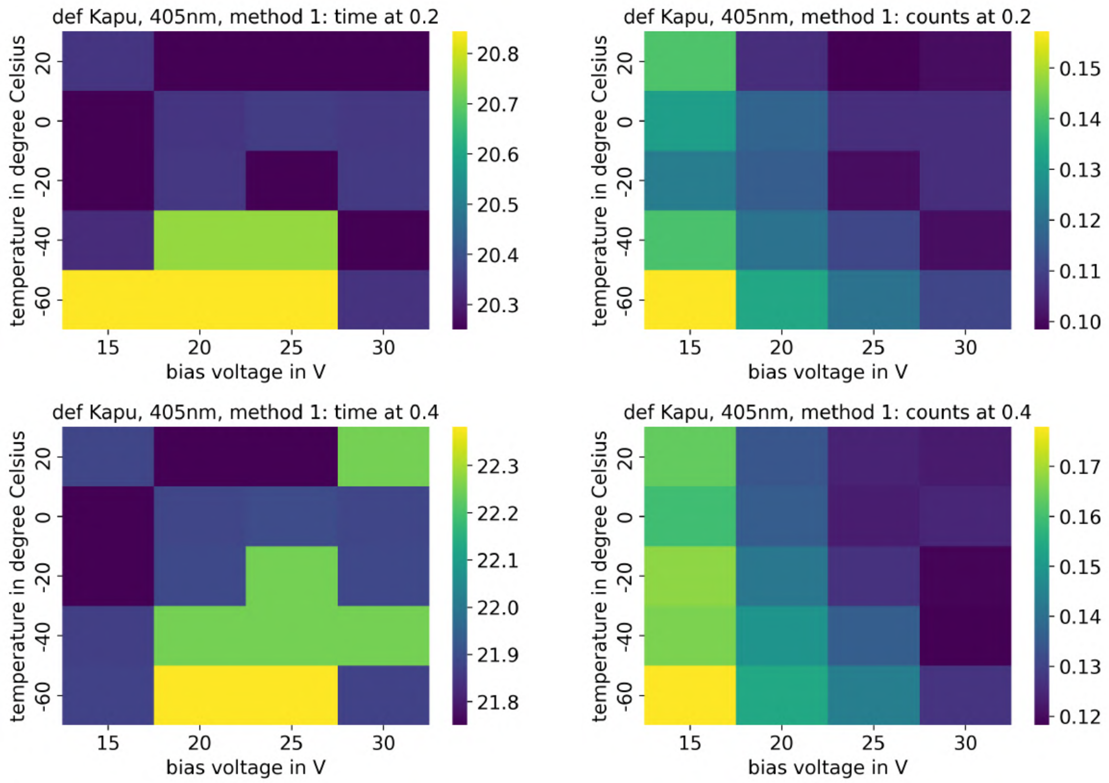

Figure A.7: Exemplary heatmaps for method 1 and the default Kapustinsky driver with the 405 nm LED. Times (in ns) are shown on the left and counts on the right. The remaining levels can be represented in the same way.

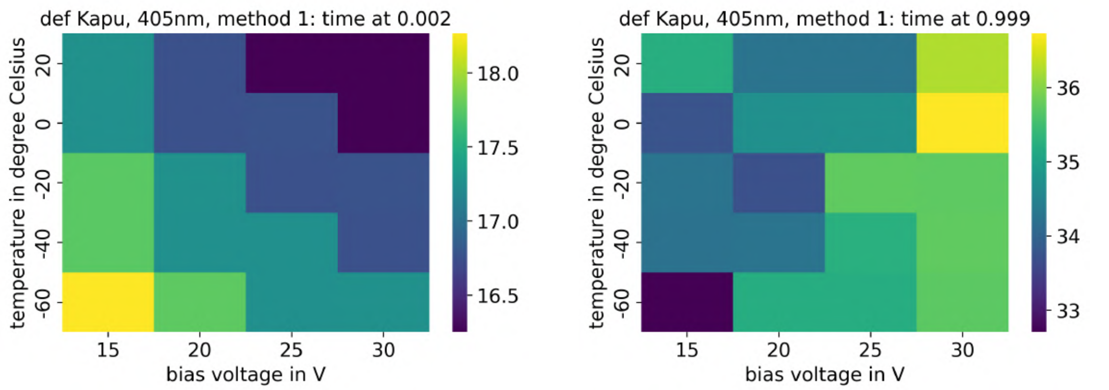

Figure A.8: Heatmaps for method 1 and the default Kapustinsky driver with the 405 nm LED depicting the times (in ns) at the beginning and the endpoint. The corresponding heatmaps for the counts are not shown, as they equal zero.

Appendix B

Bibliography

[1] B. Povh et al., *Teilchen und Kerne: Eine Einführung in die physikalischen Konzepte*, 9th ed. Berlin, Heidelberg: Springer Spektrum, 2014.

[2] P. Zyla *et al.*, “Review of Particle Physics,” *PTEP*, vol. 2020, no. 8, p. 083C01, 2020.

[3] M. Spurio, *Probes of Multimessenger Astrophysics: Charged cosmic rays, neutrinos, g-rays and gravitational waves*, 2nd ed., ser. Springer eBook Collection. Cham: Springer International Publishing, 2018.

[4] M. Aglietta et al., “On the event observed in the mont blanc underground neutrino observatory during the occurrence of supernova 1987 a,” *Europhysics Letters (EPL)*, vol. 3, no. 12, pp. 1315–1320, 1987.

[5] LIGO Scientific Collaboration and Virgo Collaboration, “Gw170817: Observation of gravitational waves from a binary neutron star inspiral,” *Physical Review Letters*, vol. 119, no. 16, p. 61, 2017. [Online]. Available: https://arxiv.org/pdf/1710.05832v1

[6] Fermi-LAT Collaboration, “Fermi-lat observations of the ligo/virgo event gw170817.” [Online]. Available: https://arxiv.org/pdf/1710.05450

[7] J. Feintzeig, “Searches for point-like sources of astrophysical neutrinos with the icecube neutrino observatory,” Dissertation, 2014. [Online]. Available: https://docushare.icecube.wisc.edu/dsweb/Get/Document-72853/Feintzeig_Thesis.pdf

[8] E. Resconi, T. Gaisser, and R. Engel, *Cosmic rays and particle physics*, second edition ed. Cambridge: Cambridge University Press, 2016.

[9] IceCube Collaboration, "Neutrino emission from the direction of the blazar txs 0506+056 prior to the icecube-170922a alert," *Science*, vol. 361, no. 6398, pp. 147–151, 2018. [Online]. Available: https://arxiv.org/pdf/1807.08794

[10] M. G. Aartsen et al., "Time-integrated neutrino source searches with 10 years of icecube data," *Physical Review Letters*, vol. 124, no. 5, p. 1084, 2020. [Online]. Available: https://arxiv.org/pdf/1910.08488

[11] E. Vitagliano, I. Tamborra, and G. Raffelt, "Grand unified neutrino spectrum at earth: Sources and spectral components," *Reviews of Modern Physics*, vol. 92, no. 4, p. 185, 2020. [Online]. Available: https://arxiv.org/pdf/1910.11878.pdf

[12] J. K. Becker, "High-energy neutrinos in the context of multimessenger physics," *Physics Reports*, vol. 458, no. 4-5, pp. 173–246, 2008. [Online]. Available: https://arxiv.org/pdf/0710.1557

[13] T. Glauch, "The origin of high-energy cosmic particles: Icecube neutrinos and the blazar case," Dissertation, 2021. [Online]. Available: https://mediatum.ub.tum.de/doc/1584755/1584755.pdf

[14] M. R. Feyereisen, I. Tamborra, and S. Ando, "One-point fluctuation analysis of the high-energy neutrino sky," *Journal of Cosmology and Astroparticle Physics*, vol. 2017, no. 03, p. 057, 2017. [Online]. Available: https://arxiv.org/pdf/1610.01607

[15] F. Henningsen, "The self-monitoring precision calibration light source for the icecube upgrade," Dissertation, 2021. [Online]. Available: https://arxiv.org/ftp/arxiv/papers/1911/1911.02016.pdf

[16] M. G. Aartsen et al., "The icecube neutrino observatory: Instrumentation and online systems," *Journal of Instrumentation*, vol. 12, no. 03, pp. P03 012–P03 012, 2017. [Online]. Available: https://arxiv.org/pdf/1612.05093

[17] I. Frank and Ig. Tamm, "Coherent visible radiation of fast electrons passing through matter," in *Selected Papers*, B. M. Bolotovskii, V. Y. Frenkel, R. Peierls, and I. E. Tamm, Eds. Berlin, Heidelberg: Springer Berlin Heidelberg, 1991, pp. 29–35.

[18] U. Katz, "Cherenkov light imaging in astroparticle physics," *Nuclear Instruments and Methods in Physics Research Section A: Accelerators, Spectrometers, Detectors and Associated Equipment*, vol. 952, p. 161654, Feb 2020. [Online]. Available: http://dx.doi.org/10.1016/j.nima.2018.11.113

[19] M. G. Aartsen et al., "Energy reconstruction methods in the icecube neutrino telescope," *Journal of Instrumentation*, vol. 9, no. 03, pp. P03 009–P03 009, 2014. [Online]. Available: https://arxiv.org/pdf/1311.4767

[20] IceCube Masterclass, "Icecube und neutrinos: Neutrinonachweis mit icecube," 2022. [Online]. Available: https://masterclass.icecube.wisc.edu/de/learn-ger/neutrinonachweis-mit-icecube

[21] J. Stachurska for the IceCube Collaboration, "First double cascade tau neutrino candidates in icecube and a new measurement of the flavor composition," *PoS-ICRC*, 2019. [Online]. Available: https://arxiv.org/pdf/1908.05506

[22] C. Spiering, "Neutrino detectors under water and ice," in *Particle Physics Reference Library: Volume 2: Detectors for Particles and Radiation*, C. W. Fabjan and H. Schopper, Eds. Cham: Springer International Publishing, 2020, pp. 785–822.

[23] M. Ackermann et al., "Optical properties of deep glacial ice at the south pole," *Journal of Geophysical Research*, vol. 111, no. D13, 2006.

[24] M. Rongen for the IceCube Collaboration, "Measuring the optical properties of icecube drill holes," *EPJ Web of Conferences*, vol. 116, p. 06011, 2016. [Online]. Available: https://www.epj-conferences.org/articles/epjconf/pdf/2016/11/epjconf-VLVnT2015_06011.pdf

[25] P. O. Hulth, "Results from the icecube video camera system at 2455 meters ice depth," *VLVnT13 - Very Large Volume Neutrino Telescope Workshop 2013*. [Online]. Available: https://indico.fysik.su.se/event/3930/contributions/4803/contribution.pdf

[26] M. Rongen, "Calibration of the icecube neutrino observatory," Dissertation, 2019. [Online]. Available: https://arxiv.org/ftp/arxiv/papers/1911/1911.02016.pdf

[27] A. Ishihara for the IceCube Collaboration, "The icecube upgrade – design and science goals," *PoS-ICRC*, 2019. [Online]. Available: https://arxiv.org/pdf/1908.09441

[28] K. Krings, E. Resconi, and M. Rongen, "The precision optical calibration module for icecube-gen2: First prototype," in *Proceedings of 35th International Cosmic Ray Conference — PoS(ICRC2017)*, I. H. Park et al., Ed. Trieste, Italy: Sissa Medialab, 10-20 July, 2017, p. 934.

[29] C. Fruck, F. Henningsen, and C. Spannfellner, "The pocam as self-calibrating light source for the icecube upgrade," *PoS-ICRC*, 2019. [Online]. Available: https://arxiv.org/pdf/1908.09600

[30] Chair of Experimental Physics with Cosmic Particles, "Experimental physics with cosmic particles," 19.02.2022. [Online]. Available: https://www.groups.ph.tum.de/cosmic-particles/experimental-physics-with-cosmic-particles/

[31] M. G. Aartsen et al., "Icecube-gen2: the window to the extreme universe," *Journal of Physics G: Nuclear and Particle Physics*, vol. 48, no. 6, p. 060501, 2021. [Online]. Available: https://arxiv.org/pdf/2008.04323

[32] K. Holzapfel, "Testing the precision optical calibration modules in the gigaton-volume-detector," Master's Thesis, 2018. [Online]. Available: https://www.groups.ph.tum.de/fileadmin/w00bya/cosmic-particles/Thesis/MA_Holzapfel.pdf

[33] F. Henningsen, "Optical characterization of the deep pacific ocean: Developement of an optical sensor array for a future neutrino telescope," Master's Thesis, 2018. [Online]. Available: https://www.groups.ph.tum.de/fileadmin/w00bya/cosmic-particles/Thesis/Master_Thesis_compressed.pdf

[34] F. Henningsen et al., "A self-monitoring precision calibration light source for large-volume neutrino telescopes," *Journal of Instrumentation*, vol. 15, no. 07, pp. P07 031–P07 031, 2020. [Online]. Available: https://arxiv.org/pdf/2005.00778

[35] T. Pertl, "Development and characterization of icecube upgrade calibration instrumentation," Master's Thesis, 2021. [Online]. Available: https://link-springer-com.eaccess.ub.tum.de/content/pdf/10.1007%2F978-3-319-96854-4.pdf

[36] J. S. Kapustinsky et al., "A fast timing light pulser for scintillation detectors," *Nuclear Instruments and Methods in Physics Research Section A: Accelerators, Spectrometers, Detectors and Associated Equipment*, vol. 241, no. 2, pp. 612–613, 1985. [Online]. Available: https://www.sciencedirect.com/science/article/pii/0168900285906229

[37] Digi-Key Electronics, "Epc9126hc epc — entwicklungsboards, -kits, programmierer — digikey," 15.03.2022. [Online]. Available: https://www.digikey.de/de/products/detail/epc/EPC9126HC/7623031

[38] Hamamatsu, "Mini-spectrometer c12880ma." [Online]. Available: https://www.hamamatsu.com/content/dam/hamamatsu-photonics/sites/documents/99_SALES_LIBRARY/ssd/c12880ma_kacc1226e.pdf

[39] IDQ, "Id100 visible single-photon detector." [Online]. Available: https://marketing.idquantique.com/acton/attachment/11868/f-0236/1/-/-/-/-/ID100_Brochure.pdf

[40] "Repo for the mongodb insert/verification scripts for the upgrade hardware," 14.03.2022. [Online]. Available: https://github.com/WIPACrepo/fatcat_db

[41] M. Holický, *Introduction to Probability and Statistics for Engineers*, 1st ed. Berlin, Heidelberg: Springer Berlin Heidelberg, 2013. [Online]. Available: https://link-springer-com.eaccess.ub.tum.de/content/pdf/10.1007%2F978-3-642-38300-7.pdf

[42] NumPy Developers, "numpy.random.uniform — numpy v1.22 manual," 07.02.2022. [Online]. Available: https://numpy.org/doc/stable/reference/random/generated/numpy.random.uniform.html